atmosphere

MDPI

Article

Weather Effects of Aerosols in the Global Forecast Model

Gill-Ran Jeong

Application Diagnostics Team, Korean Institute of Atmospheric Prediction Systems, 35 Boramaero 5-gil, Dongjak-Gu, Seoul 07071, Korea; francis7007@gmail.com

Received: 25 April 2020; Accepted: 7 August 2020; Published: 12 August 2020

Abstract: The weather effects of aerosol types were investigated using well-posed aerosol climatology through the aerosol sensitivity test of thermodynamic and hydrometeor fields, and the weather forecast performances in July of 2017. The largest aerosol direct radiative forcing (ADRF) in July was due to dust aerosols at the surface and atmosphere, and sulfate at the top of the atmosphere (TOA), respectively. The ADRF of total aerosols had unilateral tendencies in thermodynamic and hydrometeor fields. The contribution of individual aerosols was linearly additive to those of total aerosols in the heat fluxes, heating rates, humidity, and convective precipitation. However, no such linearity existed in temperature, geopotential height, cloud liquid or ice contents, and large-scale precipitation. Dust was the most influential forcing agent in July among five aerosol types due to the largest light-absorption capacity. Such unilateral tendencies of total aerosols and a part of the linearity of individual aerosols were exerted on the weather systems. The verification of medium-range forecasts showed that aerosols alleviated the overestimation of surface shortwave (SW) downward fluxes, the negative biases of temperature and geopotential heights at TOA and surface, and the underestimation in light and moderate precipitation. In contrast, they enhanced warm biases at the mid-atmosphere and underestimation in heavy precipitations, particularly negative biases in the intertropical convergence zone (ITCZ). Weather forecast scores including current aerosol information were improved in geopotential height (GPH) of the northern hemisphere (NH); however, they got worse in the temperature and the upper atmosphere GPH of the southern hemisphere (SH), which was mostly due to black carbon (BC) aerosols in the tropical regions. The missing mechanisms such as aerosol–cloud interactions, better aerosol spectral optical properties including mixing states and aging, and the near-real-time (NRT) based aerosol loading data are worthwhile to be tried in the near future for fixing the intrinsic underestimation of precipitation in ITCZ and surface radiative fluxes in the desert and biomass burning area.

Keywords: sensitivity test; weather effects; aerosol direct radiative forcing; unilateral; linearity

1. Introduction

Aerosols play essential roles in Earth's Weather and Climate by modifying radiative transfer in the atmosphere. Aerosols directly scatter and absorb the electromagnetic waves, which are called aerosol–radiation interactions and indirectly affect them by changing cloud microphysical properties such as cloud albedo or cloud lifetime, which are called aerosol–cloud interactions. The climate system perturbed by aerosols induces a radiative imbalance at the top of the atmosphere (stratosphere or tropopause), and it reaches re-equilibrium after decadal to more than a hundred years. The aerosol direct forcing is the energy available to impact the climate system with the change in global mean surface temperature. Another perturbation by aerosols is rapidly adjusted after days to weeks without affecting the global mean surface temperature. This instantaneous direct forcing affects atmospheric thermodynamic fields in the weather time scale, which renders the cloud and precipitation changes and has been referred to as the semidirect effects [1–3].

Many efforts have been made to study the climate effects of aerosols since the WCP-12 [4] suggested the insightful hypotheses on the climate changes. The IPCC has published the progress on climate changes due to aerosols such as the magnitudes of radiative forcing by total and individual aerosol types along with the distributions of aerosols emission and mass mixing ratios, and physicochemical and optical characteristics of aerosols [1]. The characteristics of aerosol properties have been unveiled not only in the emission source regions but also in transport, mixing, and aging processes. These efforts have made it possible to explore the roles of individual aerosol types in climate. The nonabsorbing aerosols such as sea salts and sulfate are paid attention because they decrease energy budget in the earth–atmospheric systems and have opposite effects on the greenhouse effects [5–7]. The absorbing aerosols such as dust and carbonaceous aerosols convert the solar radiation into thermal and moist static energy to affect regional and global dynamics and hydrological cycles [8]. The climate effects are not necessarily identical among aerosol emission sources, aerosol optical depth (AOD), and radiative forcing [1,9,10]. The interhemispheric asymmetry of aerosol emissions results in climate responses beyond aerosol emission regions [1,11]: (i) the shifts of ITCZ by sulfate aerosols and black carbon (BC) [1,10,12–14], (ii) weakening of monsoon circulation by sulfate or SO_2 emissions [15–17], and (iii) increases in temperature and precipitation due to reduction in SO_2 emission across the hemisphere while BC emissions affect localized [10,18,19]. Various climate change scenarios are examined regarding the glacial era, industrial revolution, volcano eruption, and future projections. Due to relatively small limitation of computing times and the larger time intervals of integration (~one month), climate models include the various aspects of aerosol properties: aloft emission fields of biomass burning aerosols, the vertical location of aerosol layers associated with clouds, the BC in the snow in the high altitudes or arctic regions.

In contrast, the weather effects of aerosols have been relatively less studied because the weather forecast takes a priority in fast and accurate predictions. Whereas simulating prognostic aerosols requires considerable computing time and expenses and the challengeable assimilation of initial data for aerosols fields [20]. Therefore, aerosol climatology has been alternatively used in NWP models. The main findings of weather effects appear in the local, specific events with the high aerosol concentration area, and tropical regions or monsoon regions where the intense solar radiation is available [21–23]. For instance, biomass burning events [24,25] and monsoon circulation [21,24–27]. However, the aerosol effects are not evident on a global scale, although some studies detected the large-scale mean flows related to the teleconnection between the tropical region and the extratropical regions [28]. On the other hand, Remy et al. [27] suggested interactions between aerosols and boundary layer meteorology due to feedback of aerosol radiative forcing to aerosol production mechanisms.

In terms of implementing aerosol data into NWP models, several experiments were made. Interactive aerosol models with prognostic aerosols [22,29] were tried, but the results were in noise level despite significant computational expenses. Consideration of direct and indirect radiative forcing of aerosols resulted in not explicit impacts of the indirect forcing because of high uncertainty in cloud microphysical processes [21,30]. Instead, progressing aerosol climatology is more or less promising to the improved weather forecast [26–28,31]. In particular, Bozzo et al. [23] constructed aerosol climatology ameliorated with recent observation data and data assimilation and showed significant local impacts of the regional aerosol radiative forcing. However, few studies treated the roles of the individual aerosol types in thermodynamic and hydrometeor fields and their weather effects.

Aerosol climatology was often used as an initial condition in the NWP models. It is not dynamic but static, and thus it should be logical, science-based, and as realistic as possible with the most recent information and technology. Notably, the spectral optical characteristics and atmospheric loading of aerosol types are fundamental to control the sign and magnitudes of their radiative forcing, respectively. Their products are decisive in determining the roles of aerosol types in the weather system. However, some studies used aerosol optical properties out of date, or calculated the products of spectral optical characteristics and loading data of each aerosol type without consistency [32]; one type was based on the chemical composition, and other types were based on the geographical regions.

In general, the aerosol types of geographic regions are composed of a few aerosol types of chemical composition [33,34].

To overcome the problems mentioned above with aerosol climatology in the global forecast model, we suggest well-posed aerosol climatology data. Well-posed aerosol climatology should be consistent between aerosol loading and single-particle optical properties, and among different fields such as thermodynamic and radiation fields. It leads to not only assess the aerosol–radiation interaction (ARI) but also extend to the various roles of aerosols such as aerosol–cloud interaction (ACI), surface albedo, and aerosol-chemistry interactions. We constructed a well-posed aerosol climatology by incorporating decent spectral optical properties of aerosols into the recent aerosol concentration data from observations or model outputs. Then, we implemented the well-posed aerosol climatology in the Korea Integrated Model (KIM) and evaluated aerosol radiative properties. To examine the behaviors of aerosol types in the thermodynamic and hydrometeor fields through ARI, the sensitivity to individual aerosol types was taken in the NWP model. Finally, we link the roles of aerosol species in thermodynamic and hydrometeor fields to the performance of weather forecasts.

This paper will expound as follows. Section 2 describes the configuration of aerosol climatology and the calculation of aerosol optical properties and experimental setups. The radiative properties of modeled aerosols are analyzed in Section 3. Sections 4 and 5 present the roles of aerosols in the global NWP models through sensitivity test and forecast performance, while Section 6 provides conclusions.

2. Methods

2.1. Construction of Aerosol Climatology and Implementation of Aerosols into Radiation Module

Aerosol climatology is composed of microphysical, chemical, and optical properties and loading data of aerosol types. It was implemented in the KIM through initial data of aerosol loading and look-up tables of aerosol spectral optical characteristics. *Kimaerclim* used aerosol optical characteristics embedded in the rapid radiative transfer model for global circulation models (RRTMG) [32]. Aerosol loading data was manipulated with the inverse of monthly AOD at 550 nm from Monitoring Atmospheric Composition and Climate Reanalysis (MACCRA) [35] and the three-dimensional aerosol mass concentration fields of Model for OZone and Related Chemical Tracers (MOZART) [36]. The look-up table (LUT) of aerosol spectral optical characteristics contains the relative ratio of AOD at 550 nm, single scattering albedo (SSA), and asymmetry parameter (ASY) at 14 shortwaves (SW) wavelengths [37]. However, the aerosol climatology of KIM-v3.3 (*Kimaerclim*) has inconsistency in terms of several points. First of all, aerosol optical characteristics were not consistently matched with aerosol loading data. The aerosol loading data in *Kimaerclim* are classified by chemical composition such as sea salt, dust, organic matter (OM), BC, and sulfate, while aerosol types of optical properties are classified by geographic regions such as maritime, desert, continental, urban, and volcano. Second, some aerosol optical characteristics are out of date. Besides, the aerosol optical characteristics were treated without consistency. For instance, the extinction coefficients and asymmetry parameters of desert aerosols were calculated with the refractive index of Tanré et al. [37] and the size distribution of McClatchy et al. [38]. However, its single scattering albedo was recently switched to the values calculated with refractive indices of Sinyuk et al. [39] and the size distribution of Drury et al. [40] for the improvement of NWP performances. To keep consistencies of microphysical and chemical data among desert aerosol optical characteristics, this study used the preexisting values of desert aerosols as *Kimaerclim*. The optical characteristics data of the *Kimaerclim* were compared with those of the new aerosol climatology (*Newaerclim*) that this study constructed, in Appendix A (Figures A1–A3), which was explained in Section 2.2.

Newaerclim adopted aerosol loading data from the monthly climatology of CAMSiRA (Corpernicus Atmospheric Monitoring Services Interim ReAnalysis) over the period 2003–2014 [41], which is aerosol column concentrations at 3° by 3° with a 60 model level [20]. It was provided as an initial condition and interpolated in time and space before the radiation modules of the KIM. The KIM is composed of the

nonhydrostatic dynamic core using spectral elemental methods and the physics package in the cubed sphere [42]. The vertical profiles of aerosol loading data were made by interpolation of the fraction of the total aerosol column concentrations to the KIM model grid and then its normalization to the original total aerosol column mass. The products of those aerosol species column mass concentrations and the single-particle spectral optical characteristics turned to optical properties of individual aerosol types in the radiation modules. The summations of aerosol species optical properties were combined with the optical properties of the other atmospheric components such as clouds and gaseous species, which were fed into the calculation of spectral radiative fluxes. *Newaerclim*.mod indicates the data produced by modifying the aerosol loading of *Newaerclim* (more discussion will be in Section 2.3). The three aerosol climatology data used in this study are presented in Table 1.

Table 1. Aerosol climatology data used in this study.

Name of Aerosol Climatology	Aerosol Loading	Aerosol Optical Characteristics
Kimaerclim	Monthly distribution of inverse of AOD at 550 nm based on MACCRA and MOZART grids	Inherent in RRTMG
Newaerclim	Monthly distribution of column mass concentration based on CAMSiRA	From mie calculation based on microphysical and chemical information (Table 2)
Newaerclim.mod	Monthly distribution of column mass concentration modified from CAMSiRA	From mie calculation based on microphysical and chemical information (Table 2)

2.2. Aerosol Optical Properties

The aerosol optical characteristics were calculated based on the Mie theory. Mie calculation solves the interactions between electromagnetic waves at a wavelength of λ and homogeneous spherical particles with a radius, r, and refractive index, m [43,44]. Mie theory gives the solution of the vector wave equation, including scattering amplitude functions (S) and scattering phase matrix (P) that relates the Stokes parameter of scattered radiation. S and P provide extinction and scattering factors, and asymmetry parameters. Extinction and scattering factors are obtained:

$$Q_{ext}(\lambda) = \frac{1}{s_g}\frac{4\pi}{k^2}Re\{S(\theta = 0)\} = \frac{2}{x^2}\sum_{n=1}^{\infty}(2n+1)Re[a_n + b_n] \quad (1)$$

$$Q_{sca}(\lambda) = \frac{1}{s_g}\int_0^{2\pi}\int_0^{\pi}\frac{|S(\theta,\phi)|^2}{k^2}\sin\theta d\theta d\phi = \frac{2}{x^2}\sum_{n=1}^{\infty}(2n+1)\left[{a_n}^2 + {b_n}^2\right] \quad (2)$$

where $k\left(=\frac{2\pi}{\lambda}\right)$ is the wavenumber and $x\left(=\frac{2\pi r}{\lambda}\right)$ is the size parameter. $s_g\left(=\pi r^2\right)$ is particle cross-section and Re{z} means the real part of a complex number, z. θ is the scattering angle between incident radiation and object, and ϕ is the zenith angle. $S(\theta,\phi)$ is scattering amplitude, which is expressed with Mie angular function (π_n and τ_n) and Mie coefficient (a_n and b_n). For more detail, information can be referred to in Bohren and Hoffman [45] and Boucher [3]. a_n and b_n are independent of angles but depend on x and m. The absorption factor, $Q_{abs}(\lambda)$ is obtained from the differences between extinction and scattering factors.

$$Q_{abs}(\lambda) = Q_{ext}(\lambda) - Q_{sca}(\lambda) \quad (3)$$

Single scattering albedo, ϖ_0, that is the ratio of scattering to extinction is expressed as:

$$\varpi_0(\lambda) = \frac{Q_{sca}(\lambda)}{Q_{ext}(\lambda)} \quad (4)$$

Phase function, $P(\theta)$ is equal to the element at (1,1) of the scattering phase matrix, $P_{11}(\theta)$. If we ignore the polarization of the radiation, the normalized phase function can be written as:

$$P(\cos\theta) = \frac{4}{x^2 Q_{sca}(\lambda)}\left(\left|S_1(\cos\theta)\right|^2 + \left|S_2(\cos\theta)\right|^2\right) \tag{5}$$

Asymmetry parameter, g (λ), that is the first moment of phase function, is obtained by:

$$\begin{aligned} g(\lambda) &= \frac{1}{2}\int_{-1}^{1} P(\cos\theta)\cos\theta d(\cos\theta) \\ &= \frac{4}{x^2 Q_{sca}(\lambda)}\sum_{n=1}^{\infty}\left[\frac{n(n+2)}{(n+1)}\mathrm{Re}\left(a_n a_{n+1}^* + b_n b_{n+1}^*\right) + \frac{(2n+1)}{n(n+1)}\mathrm{Re}(a_n b_n^*)\right] \end{aligned} \tag{6}$$

where z* means the conjugate of a complex number, z. Therefore, optical characteristics of single particles such as $Q_{ext}(\lambda)$, $Q_{sca}(\lambda)$, $Q_{abs}(\lambda)$, $\varpi_0(\lambda)$, $P(\theta,\lambda)$, and $g(\lambda)$ are uniquely determined by given sizes (r) and refractive index (m) of aerosols.

In the atmosphere, particle size distribution n(r), are assumed to be lognormal,

$$n(r) = \frac{dN}{dr} = \frac{1}{2}\frac{N}{\sqrt{2\pi}r\ln\sigma_g}\exp\left(-\frac{1}{2}\left[\frac{\ln\left(\frac{r}{r_0}\right)}{\ln\sigma_g}\right]^2\right) \tag{7}$$

where N is the total aerosol number. r_0 is the mean geometric radius, $\sigma_g = \exp(\sigma_o)$ is the geometric standard deviation and σ_o is the standard deviation. The mass extinction coefficients at λ, $\sigma_m^{ext}(\lambda)$ is as follows.

$$\sigma_m^{ext}(\lambda) = \frac{\int_{rmin}^{rmax} Q_{ext}\left(\frac{2\pi r}{\lambda}, m\right)\left(\pi r^2\right)n(r)dr}{\int_{rmin}^{rmax}\left(\frac{4\pi r^3}{3}\right)\rho_p n(r)dr} \tag{8}$$

where ρ_p is particle density. rmax and rmin are the maximum radius and minimum radius, respectively.

In the atmosphere, extinction aerosol optical depth and absorption aerosol optical depth at λ of aerosol type, iaer are calculated as follows.

$$\tau_{ext,iaer}(\lambda) = \int_{\text{top of atmosphere}}^{surface} \sigma_{m,\,iaer}^{ext}(\lambda)ds \tag{9}$$

$$\tau_{abs,iaer}(\lambda) = \int_{\text{top of atmosphere}}^{surface} \sigma_{m,\,iaer}^{abs}(\lambda)ds \tag{10}$$

where $\sigma_{m,\,iaer}^{ext}(\lambda)$ and $\sigma_{m,\,iaer}^{abs}(\lambda)$ are mass extinction and absorption coefficients (m^2/g) at λ of aerosol type, iaer, respectively. ds is the path length of aerosols, which is aerosol column mass in the unit of (kg/m^2). Then, AOD (absorbing aerosol optical depth (AAOD)) of total aerosols at λ, $\tau_{aer\_ext}(\lambda)$ ($\tau_{aer\_abs}(\lambda)$) is obtained by the summation of AOD (AAOD) of individual aerosols at λ:

$$\tau_{aer\_ext}(\lambda) = \sum_{iaer}\tau_{ext,iaer}(\lambda) \tag{11}$$

$$\tau_{aer\_abs}(\lambda) = \sum_{iaer}\tau_{ext,iaer}(\lambda) \tag{12}$$

Single scattering albedo of total aerosols at a wavelength of λ, $\omega_{aer}(\lambda)$ is

$$\omega_{aer}(\lambda) = \frac{\sum_{iaer} \varpi_{0_{iaer}}(\lambda)\tau_{ext,iaer}(\lambda)}{\sum_{iaer} \tau_{ext,iaer}(\lambda)} \quad (13)$$

where, $\varpi_{0_{iaer}}$ is a single scattering albedo of iaer. The asymmetry parameter of total aerosols at a wavelength of λ, $g_{aer}(\lambda)$ is

$$g_{aer}(\lambda) = \frac{\sum_{iaer} g_{iaer}(\lambda)\varpi_{0_{iaer}}(\lambda)\tau_{ext,iaer}(\lambda)}{\sum_{iaer} \varpi_{0_{iaer}}(\lambda)\tau_{ext,iaer}(\lambda)} \quad (14)$$

where, g_{iaer} is the asymmetry parameter of iaer. $\tau_{ext,iaer}(\lambda)$ and $\tau_{abs,iaer}(\lambda)$ are linearly additive to $\tau_{aer\_ext}(\lambda)$ and $\tau_{aer\_abs}(\lambda)$. On the other hand, $\omega_{aer}(\lambda)$ and $g_{aer}(\lambda)$ are weighted by sums of scattering intensity of individual aerosols.

Sizes and compositions of five aerosol types were referred to as CAMS-based aerosol climatology [20], as shown in Table 2. Sea salt and dust have three size bins in nucleation, accumulation, and coarse modes. Sea salt has a bimodal distribution, while dust, organic matter (OM), black carbon (BC), and sulfate have monomodal distribution. OM is assumed as the external mixtures of water-soluble, water-insoluble, and soot aerosols, with the mixing ratio of 84:13:3 [20]. External mixing keeps the microphysical and chemical characteristics of the individual aerosol species in a mixture. However, internal mixing makes a mixture with new microphysical and chemical characteristics that differ from the original ones of individual aerosols. External mixtures were reported as less absorbing than internal mixtures to be assumed, such as core–shell or homogeneous mixing types [46–49]. Although the modeled internal mixtures were not exactly the same as the observed in the atmosphere, the absorption intensity of core–shell types was reported as that of between external mixtures and homogeneous mixing types [49]. The refractive indices of aerosol chemical composition, the sizes of aerosols, and mixing states are essential factors determining the light absorption of aerosols [46]. The aerosol absorption is also affected by the hygroscopicity that changes the sizes and compositions of dry aerosols. We assumed that all sea salt and sulfate aerosols are in 80% relative humidity (RH). Hydrophobic and hydrophilic parts of carbonaceous aerosols were supposed in 20% RH and 50% RH, respectively.

Table 2. Aerosol microphysical and chemical characteristics used in new aerosol climatology (*Newaerclim*). (GPCP: Global Aerosol Climatology Project).

Aerosol Type	Size Bin	Density, ρ (kg/m^3)	Mode Radius, r_{mod} (μm)	Geometric Standard Deviation, σ_g	Refractive Indices
Sea salt	0.03–0.5 0.5–5.0 5.0–20.0	1.183×10^3	0.1992 1.992	1.9 2.0	OPAC [34]
Dust	0.03–0.55 0.55–0.9 0.9–20.0	2.61×10^3	0.29	2.0	Woodward [50]
Black carbon	0.005–0.5	1.0×10^3	0.0118	2.0	OPAC [34] (SOOT)
Sulfate	0.005–20.0	1.8×10^3	0.0212	2.24	Lacis [51] (GACP)
Organic matter	0.005–20.0 The external mixture of water-soluble (WASO), insoluble (INSO), and soot (SOOT)	1.8×10^3 2.0×10^3 1.0×10^3	0.0212 0.471 0.0118	2.24 2.51 2.0	OPAC [34] OPAC [34] OPAC [34]

Figure A1 presents the Mie calculations of *Newaerclim* in blue lines. All aerosol optical properties were interpolated/extrapolated into 14 SW bands in RRTMG. Aerosol optical characteristics of *Newaerclim* were compared with those of *Kimaerclim* (black line) [4,47]. There were distinct differences between them. First, the classification standard of aerosol types is the chemical composition in

Newaerclim but geographic regions in *Kimaerclim*. The inconsistency in aerosol types between aerosol loading and aerosol optical characteristics causes unreasonable optical properties in *Kimaerclim*. SSA of urban aerosols at 532 nm matching with BC loading is too high 0.78 than the well-known BC data (0.3–0.35) [34] (Figure A2). The asymmetry parameter of urban aerosols has a smaller spectral dependency in the range of 0.6–0.8 than the asymmetry parameter of BC in *Newaerclim* in the range of 0.0–0.7 (Figure A3). Second, extinction characteristics in *Newaerclim* indicate a mass extinction coefficient (m^2/g), but in *Kimaerclim* represents the ratio relative to the inverse of AOD at 550 nm (unitless) (Figure A1). Third, *Newaerclim* uses more realistic size spectra such as three size bins (fine, accumulate, coarse) for sea salts and dust aerosols, but *Kimaerclim* uses one size bin for maritime and desert aerosols. Fourth, some aerosol optical properties in *Kimaerclim* are out of date. SSA of dust-like at 532 nm is as low as 0.75, much lower than *Newaerclim* dust SSA (0.96, 0.90, and 0.84). It implies that dust-like of the *Kimaerclim* is more absorbing than the dust of the *Newaerclim*.

2.3. Evaluation of AOD and AAOD

The modeled AOD ($\tau_{aer\_ext}(\lambda)$) and AAOD ($\tau_{aer\_abs}(\lambda)$) were evaluated by AERONET (AErosol RObotic NETwork), MODIS (MODerate resolution Imaging Spectroradiometer) [52], and MISR (Multiangle Imaging Spectroradiometer) [53] data (2003–2017). AERONET was version 3.0, and with level 2.0 data from automatically cloud cleared and quality assured prefield and postfield calibration applied (https://aeronet.gsfc.nasa.gov/cgi-bin/data_display_inv_v3). Eighteen AERONET sites were selected as the location where both AOD and AAOD were available.

MODIS is onboard Aqua that is at 1:30 p.m. ascending node, sun-synchronous, and near-polar orbit. The MODIS_AOD indicates global coverage monthly data derived from MODIS level 3 daily mean data of Combined Dark Target and Deep Blue AOD at 550 nm for land and ocean. MISR is onboard Terra. The MISR AOD indicates level 3 Global Aerosol product covering a one-month period such as the optical depth average.

For the comparison of modeled AOD and AAOD with observations, interpolation/extrapolation of modeled AOD, MODIS_AOD, and MISR_AOD were made concerning 18 AERONET sites. At most AERONET sites, modeled AODs were in good agreement with monthly variations of three observed AODs. Modeled AAOD agreed well with AERONET_AAOD. Figure 1 shows the scatter plots of AOD and AAOD, and the model results mostly agree with AERONET observations within a factor of two. The linear regression analysis turned out that modeled AOD and AAOD was in good and moderate agreement with AERONET observations as correlation coefficients of 0.807 and 0.631, respectively. Monthly variations of modeled AOD and AAOD of individual aerosols were shown in Figure 2. Dust and sea salt were out of phase, and BC aerosols were the smallest fractions of total AOD. Total AOD peak appeared in May when dust emission was dominant, and the second peak appeared in September when biomass burning was dominant. As for the monthly variations of AAOD, the peak appeared in September due to BC absorption.

On the other hand, *Newaerclim* revealed a few shortcomings. In the site-comparisons with AERONET data, the modeled AODs overestimated in the summer months at such sites as Banizoumbou, Beijing, Carpentras, Cartel, Ispra, Mexico_City, Sede Boker, and Venise, while they underestimated in winter months. Also, the verification of SW downward fluxes with Clouds and Earth's Radiant Energy System (CERES) turned out to be a dominant underestimation in the desert area (shown in Section 5). It was partly related to the overloading of dust aerosols in CAMSiRA climatology [20]. To obtain the better values of AOD and improve the biases in radiative fluxes, we tried to modulate the dust loadings and produce *Newaerclim.mod*. We did a curve-fitting to the monthly dust loadings with maximum reduction by 29% in May, and maximum increment by 22% in December. As a result, the monthly variation of modeled AOD turned to double peaks in May and September. The correlation coefficients of AOD and AAOD between the modeled and AERONET improved as 0.863 and 0.693, respectively. When it came to underestimating SW downward radiative fluxes against the Clouds

and Earth's Radiant Energy System (CERES), *Newaerclim.mod* was improved than *Newaerclim* in July (shown in Section 5).

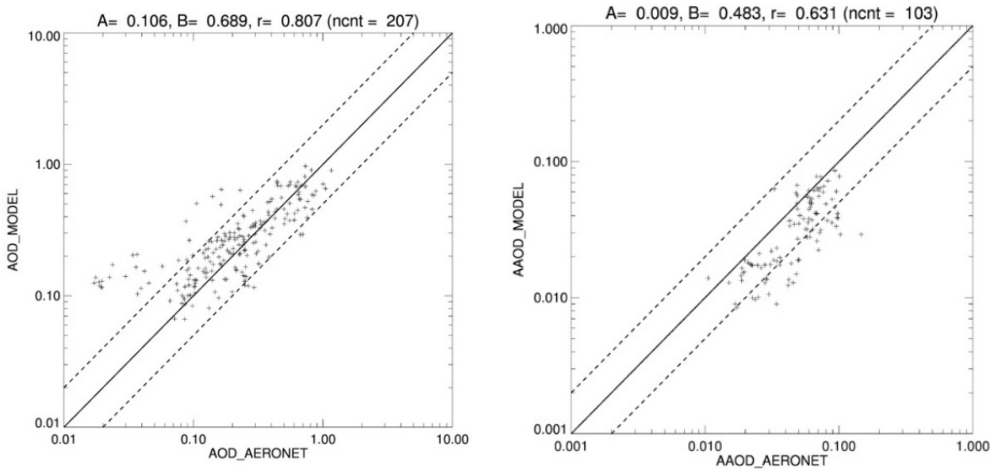

Figure 1. Scatterplots of the modeled (**a**) aerosol optical depth (AOD) and (**b**) absorbing aerosol optical depth (AAOD) at 550 nm against AERONET observations. Ncnt indicates the number of observations. r is the correlation coefficient. B is a slope. A is the y-intercept. The 1:1 line (solid) and 1:2 line (dashed) are inset.

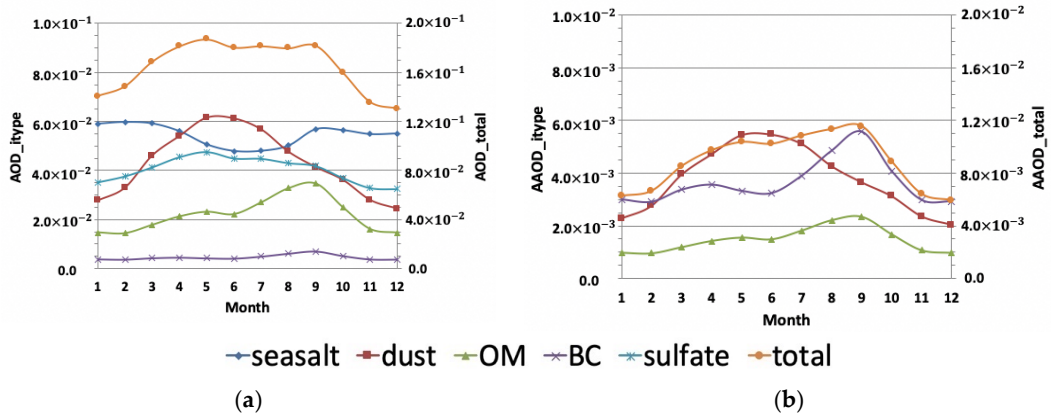

Figure 2. Monthly variation of (**a**) AODs and (**b**) AAODs at 532 nm of CAMSiRA aerosol climatology. The left axis is AOD and AAOD of individual aerosol types (itype), and the right axis is AOD and AAOD of total aerosols.

2.4. Experimental Setup

The behaviors of individual aerosols in atmospheric thermodynamic and hydrometeor fields were examined through sensitivity tests. Each aerosol species was added to the aerosol-free conditions in the KIM and its effects on the thermodynamic and hydrometeor fields were analyzed. The sensitivity results of a 10-day forecast simulation were provided to find the role of aerosol species in the medium-range weather forecasts. Then, we verified a medium-range forecast with aerosol climatology in July of 2017. July and January were conventionally used to verify the medium-range forecast in the KIM as representative months of boreal summer and winter. This study chose July when aerosol loading is more abundant, and solar radiation is more intense than January, in the northern hemisphere, for the distinct signals.

The experimental setups are presented in Tables 3 and 4. The experimental names for sensitivity tests are lower letters such as **noaer** and **newaer**, while those for the verification of medium-range forecasts are upper letters such as **NOAer** and **NewAer**. The NWP model is used with KIM-v3.3

that comprises the dynamic core and physics package. Physics module contains a rapid radiative transfer model for general circulation models (RRTMG)-based radiation [54], Noah-based land surface model [55], Yonsei University (YSU)-based planetary boundary layer [56], KIM-Arakawa-based orographic gravity wave [57], Simplified Arakawa-Schubert (SAS)-based deep-convection [58], SAS-based shallow convection [59], WRF Single Moment 5-class (WSM5)-based microphysics [60,61], and Tiedtke-based cloudiness [62].

Table 3. Experimental setups for sensitivity test to aerosol types (a 10-day forecast simulation). x indicates a specific aerosol species such as sea salt, dust, organic matter (OM), black carbon (BC), and sulfate.

Exp. Name	Aerosol Climatology
noaer	
newaer_all	*Newaerclim* including all types of aerosols
newaer_x	*Newaerclim* including aerosol type, x

Table 4. Experimental names along with aerosol climatology for the verification of medium-range forecasts in the Korea Integrated Model (KIM) (31 ensemble simulations).

Exp. Name	Aerosol Climatology
NOAer	
KIMAer	*Kimaerclim*
NewAer	*Newaerclim*
NewAer.mod	*Newaerclim.mod*

For the sensitivity to aerosol types, we did experiment on the one 10-day forecast starting at 00:00 UTC on 1 July in 2017 with ne180np3 resolution (approximately 12 km grid spacing). The fifth generation of ECMWF atmospheric reanalysis of the global climate (ERA5) [63] were used as Initial and boundary conditions for atmosphere, and the National Center for Environmental Prediction (NCEP) Global Forecast System (GFS) analysis [64] for sea surface temperature (SST) and sea ice. **noaer** of the aerosol-free simulation was used as a control run. Then, we simulated **newaer_all** and **newaer_x** by adding column mass loading of each aerosol type of aerosol climatology, *Newaerclim*, to **noaer**, as shown in Table 3.

For medium-range forecasts, 31-member ensembles of 10-day forecasts were simulated from every 00:00 UTC in July 2017 with the same model resolution, and initial and boundary conditions as those in sensitivity experiments. The four medium-range forecast experiments were carried out with different aerosol climatology (Table 4). The control run was **NOAer** with no aerosol climatology. **KIMaer**, **NewAer**, and **NewAer.mod** use *Kimaerclim*, *Newaerclim*, and *Newaerclim.mod*, respectively. For the verification of medium-range forecasts, the Clouds and Earth's Radiant Energy System (CERES), radiosonde, Automatic Weather Station (AWS) data in Korean Peninsula, and the Climate Prediction Center (CPC) ([65]), and the Tropical Rainfall Measuring Mission (TRMM) Multisatellite Precipitation Analysis (TMPA) [66], were used. We assessed the biases and errors regarding meteorological factors and estimated the forecast score using the KIM self-analysis fields.

3. Radiative Effects of Aerosols

To analyze aerosol–radiation interactions, we produced aerosol loading in optics units and the radiative forcing at Earth–atmospheric systems. The radiative effects were calculated in the experiment of the 10-day forecast in Table 3, starting at 00:00 UTC on 1 July in 2017 and January 1 in 2017. Figure 3 shows the AOD, AAOD, and scattering AOD (SAOD). The global means of aerosol optical depths in July were larger than those in January by a factor of 1.3, 1.7, and 1.3 for AOD, AAOD, and SAOD, respectively. The fractions of AAOD to AOD were 0.06 in July and 0.04 in January. The distribution AOD in July was distinct in the desert area of Sahara, western India, and the Taklamakan. The primary

sources of absorbing aerosols were deserts of the northern hemisphere (NH) and biomass burning regions in central Africa. The sources of AOD in January moved further southward than those in July, and the main AAOD regions are the central western coast of Africa, Bangladesh, and the east coast of China.

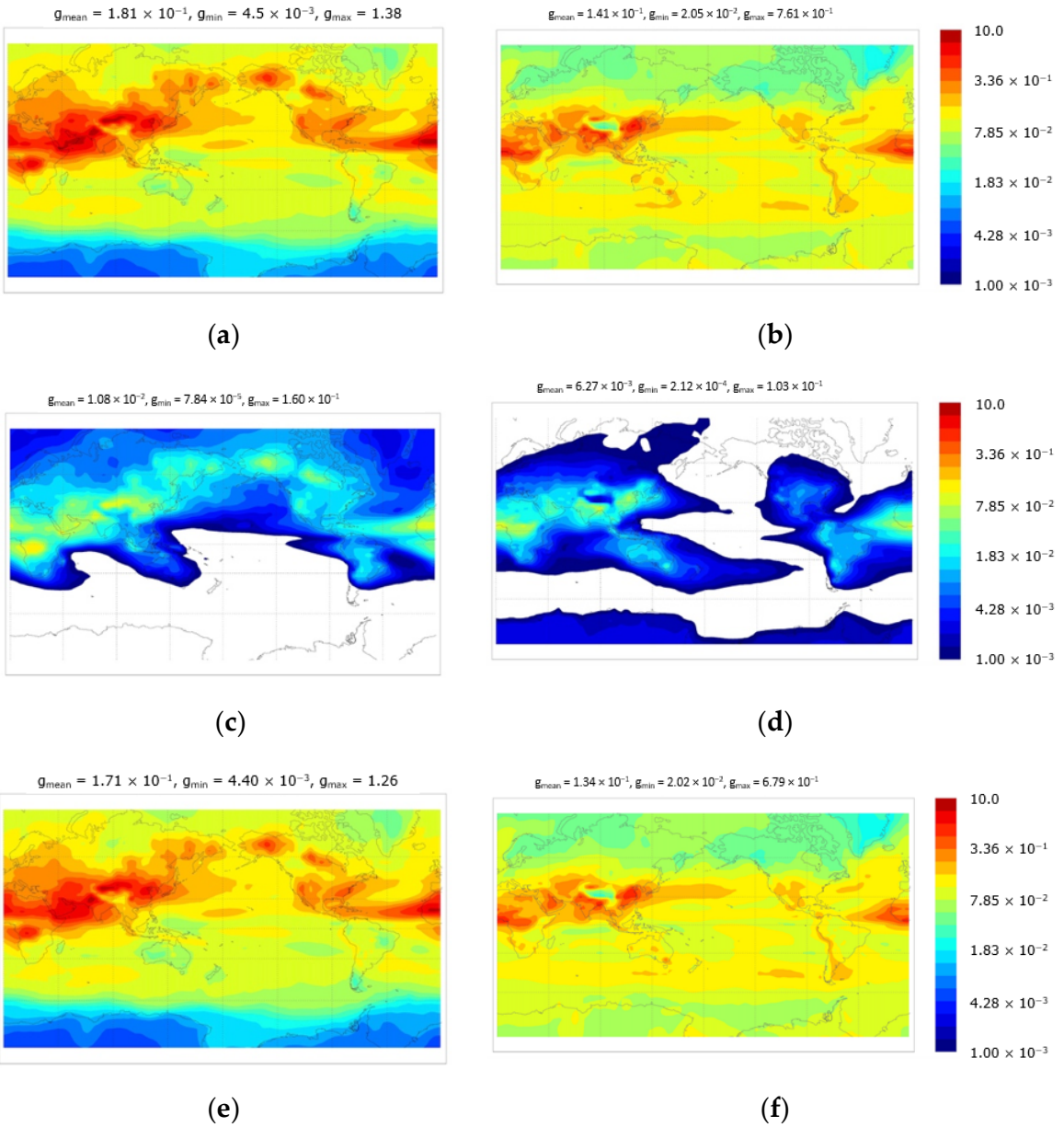

Figure 3. The distributions of (**a**,**b**) AOD, (**c**,**d**) AAOD, and (**e**,**f**) scattering AOD (SAOD) in July (first column) and January (second column).

Radiative forcing is a direct measure of the amount that the Earth's energy budget is out of balance, and it is vital to give the idea how much various radiative forcing agents affect the weather and climate system since industrialization in 1750. Among radiative forcing agents, aerosols are difficult to assess the radiative forcing due to the most significant uncertainties that stem from the inhomogeneous distribution of an aerosol amount in space and time, composition and radiative properties, radiative transfer, the dependence of the forcing calculation on clouds or surface albedos, retrieval errors of remote sensing measurements, and non-aerosol-related errors ([1], reference therein).

Aerosol radiative forcing due to aerosol–radiation interaction (RFari) is the changes in net irradiances at tropopause as stratospheric temperature profiles adjust to an equilibrium state, resulting

in earth surface temperature changes [2]. However, it recently included the rapid adjustment processes in which forcing mechanism affects cloud cover or the other components of the earth–atmospheric system during a short period (a few hours to a few weeks). The sum of RFari and the rapid adjustment processes is called effective radiative forcing from aerosol–radiation interactions (ERFari) [3]. RFari was estimated as -0.35 ± 0.5 Wm^{-2} [1] from reanalysis estimates [67], and observational studies [68], with uncertainties mentioned above. Rapid adjustment to aerosol–radiation interactions was assessed as a best estimate of -0.1 Wm^{-2} [69] in the uncertainty of -0.3 to $+0.1$ Wm^{-2} with a 5% to 95% range [70]. Therefore, the overall assessment for ERFari is -0.45 ± 0.5 Wm^{-2} [1].

The aerosol direct radiative forcing (ADRF) in this study is more likely applicable to the one due to ERFari. However, the ADRF in this study using 10-day forecast data may not be directly compared with those in climate models assessed as global annual mean values. We calculated ADRF as follows. Direct radiative forcing from atmospheric aerosols, ΔF, is defined as the difference in the energy levels between a situation where aerosols are present, F_A, and a situation where these atmospheric particles are absent, Fc (Equation (15)). The ADRF was analyzed at the top of atmosphere (TOA), the atmosphere (ATM), and the surface (SFC).

$$\Delta F_{isky,ilevel} = \left(F^{\downarrow A}_{isky,ilevel} - F^{\uparrow A}_{isky,ilevel}\right) - \left(F^{\downarrow C}_{isky,ilevel} - F^{\uparrow C}_{isky,ilevel}\right) \quad (15)$$

where isky indicates the sky conditions such as "clr" for clear-sky and "all" for all-sky. ilevel indicates TOA or SFC. The arrows indicate the direction of the global fluxes: $\downarrow$ is downward flux and $\uparrow$ is upward flux. The direct radiative forcing at the atmosphere is the difference between TOA and SFC. The ADRFs at ATM in clear-sky and all-sky are calculated as $\Delta F_{clr,ATM}$ and $\Delta F_{all,ATM}$, respectively:

$$\Delta F_{isky,ATM} = \Delta F_{isky,TOA} - \Delta F_{isky,SFC} \quad (16)$$

The sign of ΔF implies that negative values are associated with aerosol cooling, and positive values are associated with aerosol warming at each level.

The magnitudes of ADRF in the clear sky were larger than those in all-sky because the radiative effects of clouds were added to the modification of radiative transfer. In this study, the ADRFs in July were more significant than those in January, by a factor of 1.3, 2.1, and 1.6 at TOA, ATM, and SFC, respectively. The differences in the ADRFs between July and January were the smallest at TOA, but the differences were the largest at ATM. The signs of ADRF imply the gain of SW radiation at the atmosphere but the loss of SW radiation at the surface and the top of the atmosphere. Such differential vertical structures of ADRF were linked with the horizontal distributions of aerosol optical properties, particularly with aerosol sources. The most significant contributing species to ADRF in July at the surface and atmosphere were dust, and those at TOA were sulfate (Figure 4a). When it came to aerosol optical properties, the largest AODs and AAODs were attributed to dust aerosols in desert areas. In contrast, the most dominant contributors to ADRF in January at surface and TOA were sea salt, while those in the atmosphere were black carbon (Figure 4b). The largest AODs and AAODs were due to sea salts from the ocean and BC aerosols from anthropogenic sources, respectively.

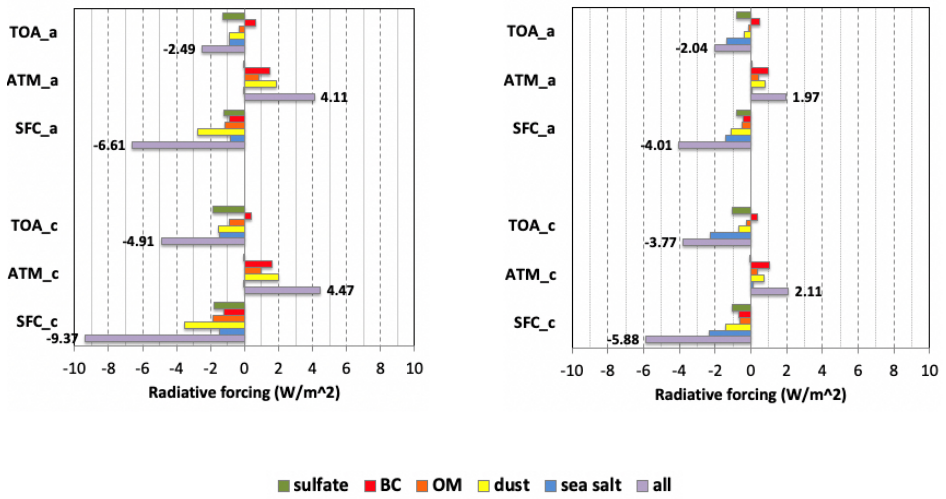

Figure 4. The global means of aerosol direct radiative forcing for a 10-day forecast starting from (**a**) 1 July and (**b**) 1 January of 2017. _a indicates all-sky, and _c indicates a clear sky.

4. Sensitivity in Thermodynamic and Hydrometeor Fields

The individual aerosols exert different radiative forcing in terms of its sign, magnitudes, and spatial distribution. The radiative forcing is not necessary to appear to the aerosol source regions [1,9,71], and weather effects of aerosols are not directly related to the aerosol source region, either. The individual aerosols radiative forcing is smaller than total aerosols forcing, and the impacts of individual aerosols on the weather forecast performance may not be distinguishable. For this reason, we tried to examine the responses of individual aerosols to the thermal and hydrometeor fields and to get useful information about the roles of specific aerosol types in the NWP models.

For the effects of aerosols on thermodynamic fields, the changes in sensible heat fluxes (SHflx), latent heat fluxes (LHflx), and PBL height (hpbl) relative to **noaer** were investigated (Figure 5). Due to the reduced radiative fluxes, the surface temperature decreased, and stability in the lower atmosphere increased. Thus, the turbulent mixing of SHflx and LHflx decreased, resulting in boundary layer structures of wet surfaces and dry above. Overall, Earth's surface became cold and wet due to aerosols; however, it got too warm and wet due to BC aerosols. Among five types of aerosols, dust aerosols made the most contributions to the changes in heat fluxes and atmospheric stability. Sea salt aerosols made fewer contributions to the thermodynamic field than any other aerosol types in July.

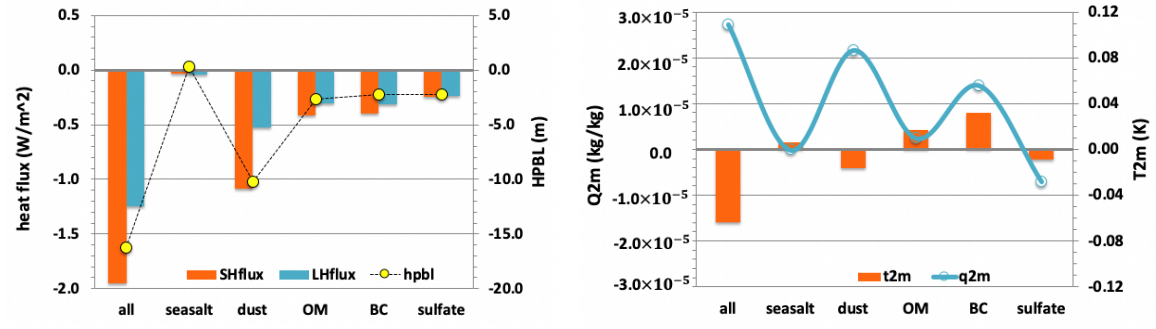

Figure 5. The sensitivity of the surface thermal fields to aerosol types. The changes in (**a**) Sensible heat flux (Shflux), latent heat flux (Lhflux), and PBL height (hpbl) and (**b**) temperature at 2m (t2m) and specific humidity at 2 m (q2m) relative to aerosol-free conditions, for a 10-day forecast starting from 1 July of 2017.

Unlike negative surface radiative forcing, positive atmospheric radiative forcing affected vertical profiles of atmospheric thermodynamic and hydrometeor fields (Figure 6). Due to the less moisture mixing at the lower atmosphere and the evaporation in a warmer atmosphere, the differences in specific humidity (Q) had transition points about 800 hPa. Below 500 hPa, SW heating rates (SWhr) increased due to absorption by aerosols, and the longwave (LW) cooling rates increased due to increments of LW fluxes emitted from Earth's surface and clouds out to space. The cold and wet surface but the warm and dry atmosphere made the cloud water content (Qc) increase below 700 hPa and decrease above. In particular, the maximum of Qc appeared at 900 hPa because drying and warming atmosphere caused more evaporation of water vapor and stabilized the boundary layer to lower its top, while the abundance of water vapor caused to lower lifting condensation levels (LCL), so-called cloud-top thinning and cloud-bottom thickening (Figure 6b). Such a pattern of Qc was similar types of cloud cover profiles that Persad et al. [72] found when BC aerosols were assumed to exist in the boundary layer [72], Figure 4c of tropical regions. It was caused by the light-absorption by BC aerosols without consideration of the indirect effects of BC. The aerosol also reduced the cloud cover above the mid-level atmosphere and decreased cloud ice content (Qi) at the entire atmosphere.

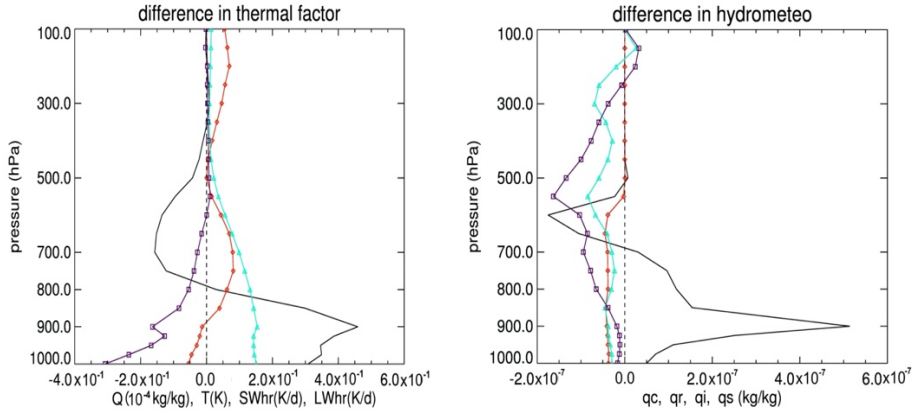

(**a**) (**b**)

Figure 6. Vertical profiles of the global mean of the differences in (**a**) thermal factors such as shortwave (SW) heating rates (SWhr) in cyan, longwave (LW) heating rates (LWhr) in purple, temperature (T) in red, and specific humidity (Q) in black (**b**) hydrometeors such as cloud liquid water content (Qc) in black, rainwater content (Qr) in red, cloud ice contents (Qi) in cyan, and snow content (Qs) in purple, from aerosol-free conditions for a 10-day forecast starting from 1 July of 2017. Dotted lines indicate changes of zero.

Thus, precipitation such as rain (Qr) and snow (Qs) mixing ratios decreased when compared to the aerosol-free conditions.

The changes in thermodynamic and hydrometeor fields of individual aerosols cases (**newaer_x**) were smaller than those of total aerosols cases (**newaer_all**) (Figures 7 and 8) and they depended on their concentrations and optical properties. Figure 7 shows that the differences in heating rates pretty linearly responded to the absorption capacities of individual aerosol types. Dust made the most contribution to the changes in SW heating rates and LW heating rates in July among aerosol species. In contrast, the differences in temperature of **newaer_all** increased with the double-positive peaks at the lower and upper atmospheres. Such temperature differences appeared in **newaer_dust** and **newaer_BC**. However, temperature differences became negative due to sulfate in the entire atmosphere and dust below 900 hPa. It turned out that the decreases in temperature at the lower atmosphere were due to scattering by dust and sulfate, whereas the increases in temperature above the mid-level atmosphere were due to absorption by dust and black carbon.

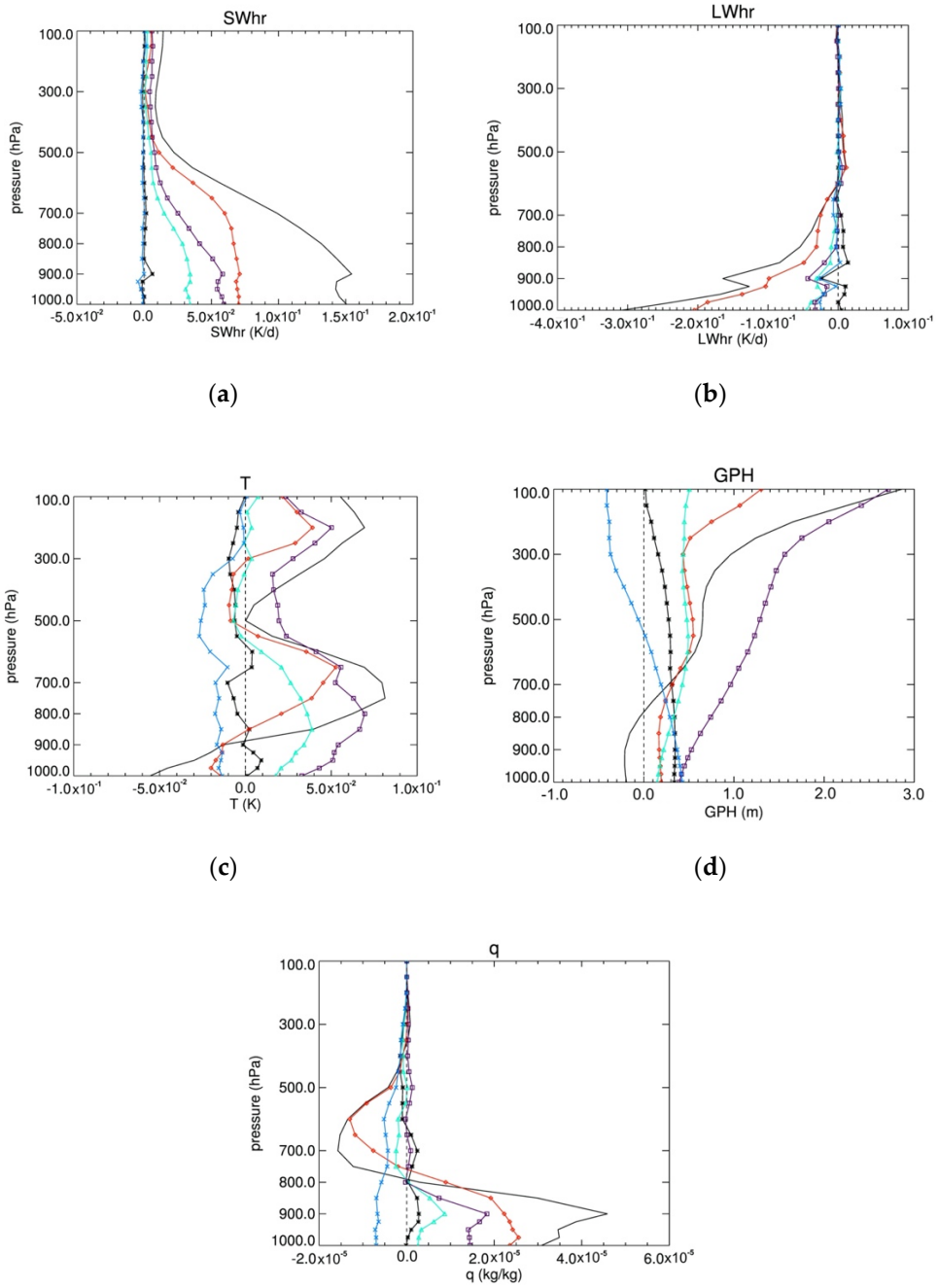

Figure 7. The sensitivity of thermal fields such as (**a**) SW heating rates, (**b**) LW heating rates, (**c**) temperature, (**d**) GPH, and (c) specific humidity to aerosol types in the 10-day forecast of 1 July of 2017. Aerosol types are all types of aerosols (black with no symbol), sea salt (black), dust (read), OM (cyan), BC (purple), and sulfate (blue). Dotted lines indicate changes of zero.

On the other hand, the differences in geopotential height (GPH) relative to aerosol-free conditions were determined by thermal information accumulated from the bottom of the atmosphere (Figure 7). All the individual aerosol cases (**newaer_x**) increased GPH except sulfate (**newaer_sulfate**). GPH differences were negative at the surface due to the cooling of dust and sulfate aerosols, and they were positive above the mid-atmosphere due to the heating of absorbing aerosols. The most significant contributor to GPH changes in July was BC, which had the most potent absorption characteristics among aerosol composition. As for the difference in specific humidity relative to **noaer**, most aerosol

types had positive changes in the lower atmosphere and negative changes in the mid-atmosphere. Among five aerosol types, the dust seemed to be the most influential on the changes due to total aerosols (**newaer_all**), which were moistened at a lower atmosphere and dry at mid-level atmosphere. In contrast, sulfate made the atmosphere cool and dry as the same as its surface impacts (shown in Figure 5b) even though it made a smaller contribution to the changes in the specific humidity than any other aerosol species.

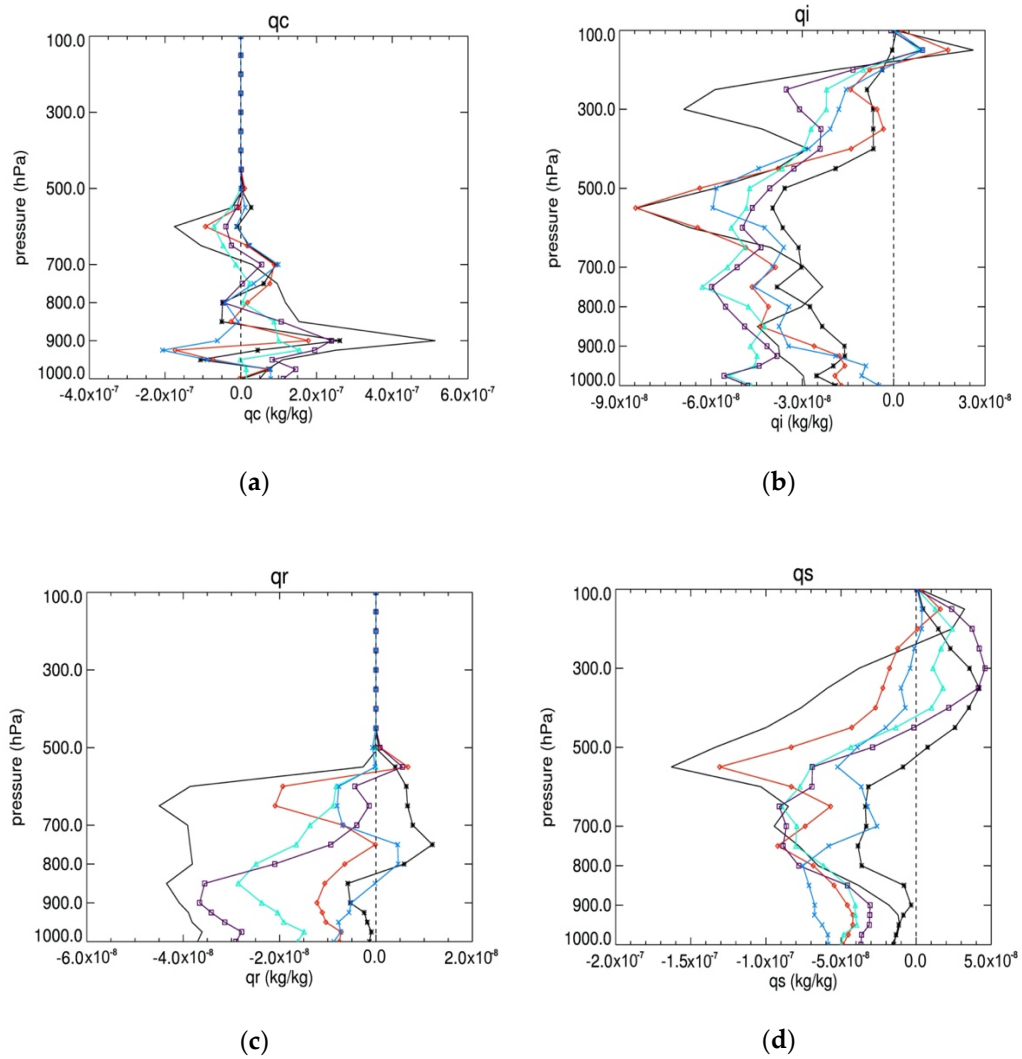

Figure 8. The sensitivity of hydrometeors such as (**a**) qc, (**b**) qi, (**c**) qr, and (**d**) qs to aerosol types in the 10-day forecast of 1 July of 2017. Aerosol types are all types of aerosols (black with no symbol), sea salt (black), dust (read), OM (cyan), BC (purple), and sulfate (blue). Dotted lines indicate changes of zero.

Figure 8 shows how specific aerosols change the hydrometeor relative to aerosol-free conditions(**noaer**). Most aerosol species increased cloud liquid water contents (Qc) at the lower atmosphere and decreased Qc at the mid-atmosphere (Figure 8b). The Qc changes of individual aerosols were not linearly additive to those of the **newaer_all**. Instead, the vertical profiles of Qc differences in **newaer_all** were similar to those in absorbing aerosols such as dust, BC, and OM. The changes in cloud ice content (Qi) profiles of **newaer_all** were close to the mean values of those in individual aerosols (**newaer_x**) in the lower atmosphere (Figure 8b). However, Qi profiles of **newaer_all** at 550 hPa and 300 hPa were affected by dust and BC aerosols, respectively.

The differences in rainwater content (Qr) in **newaer_x** were negative below 500 hPa except those in **newaer_seasalt**. Qr decreased in the lower atmosphere due to BC and OM and in the mid-atmosphere

due to dust. As for the changes in snow content (Qs) profiles, all types of aerosols in **newaer_x** decreased Qs most substantially around 700 hPa as compared to **noaer**. The dust case showed considerable negative changes at 550 hPa, which was similar to the case of **newaer_all**. However, BC, OM, and sea salt increased Qs above 500 hPa due to the pleasant condition to form ice nuclei. Such features of hydrometeor fields due to aerosol species appeared in the global precipitation changes (Figure 9). Overall, the global changes in convective precipitation (PRECC) were induced by absorbing aerosols such as dust, BC, and OM in decreasing order. The negative changes in PRECC of **newaer_x** were linearly additive to those of **newaer_all**. In contrast, the global changes in large-scale precipitation (PRECL) were affected by most aerosol types.

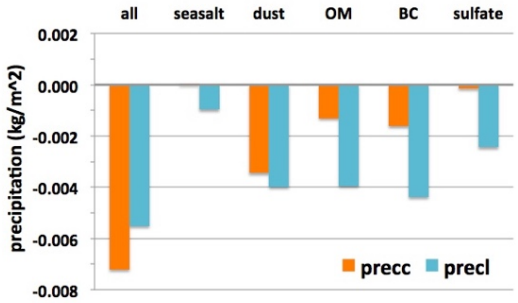

Figure 9. The sensitivity of precipitation to aerosol types. The changes in convective precipitation (PRECC) and large-scale precipitation (PRECL) relative to aerosol-free conditions for a 10-day forecast starting from 1 July of 2017.

The differential radiative fluxes with altitudes caused changes in thermodynamic fields. Through ARIs, aerosols tended to change the vertical gradients of temperature and humidity and to stabilize the atmosphere, leading to making the atmosphere with fewer clouds and less precipitation with respect to **noaer**. The differences due to individual aerosols were linearly additive to those due to total aerosols in heat fluxes, heating rates, humidity, and PRECC; however, they were not linear in temperature, geopotential height, and cloud liquid or ice contents, and PRECL. Dust was the most influential on the direct and semidirect effects of aerosols in July, among absorbing and nonabsorbing aerosols.

5. Weather Effects of Aerosols

To find the impacts of aerosols on weather forecasts, ensemble simulations of 10-day forecasts from 1 July to 31 July 2017, were verified. Figure 10 shows the differences in SW downward radiation in the 54–72 h forecast against CERES in **NOAer**, **KIMAer**, **NewAer**, and **NewAer.mod**. In clear-sky, **NOAer** showed the positive biases in the entire Earth's surface, particularly, desert areas. Adding aerosols to **NOAer** made such positive biases disappear, rather negative biases turned out in the west Indian ocean and downwind of the Saharan desert. The global mean biases in the experiment with aerosol climatology decreased by up to 99% as compared with those in **NOAer**, and the global mean root mean square errors (RMSEs) decreased by more than 50% (Table 5). In the **KIMAer** negative biases over the ocean and the Arctic regions appeared due to the scattering by the overloading of sea salt aerosols. On the other hand, most biases were reduced particularly over the ocean in the **NewAer**, while negative biases appeared over northern Africa, western India, and Taklamakan desert. In **NewAer.mod**, negative biases over the desert reduced, but the rest of the negative biases remained due to absorption by BC aerosols. However, the global mean of the biases was smallest in **NewAer.mod**.

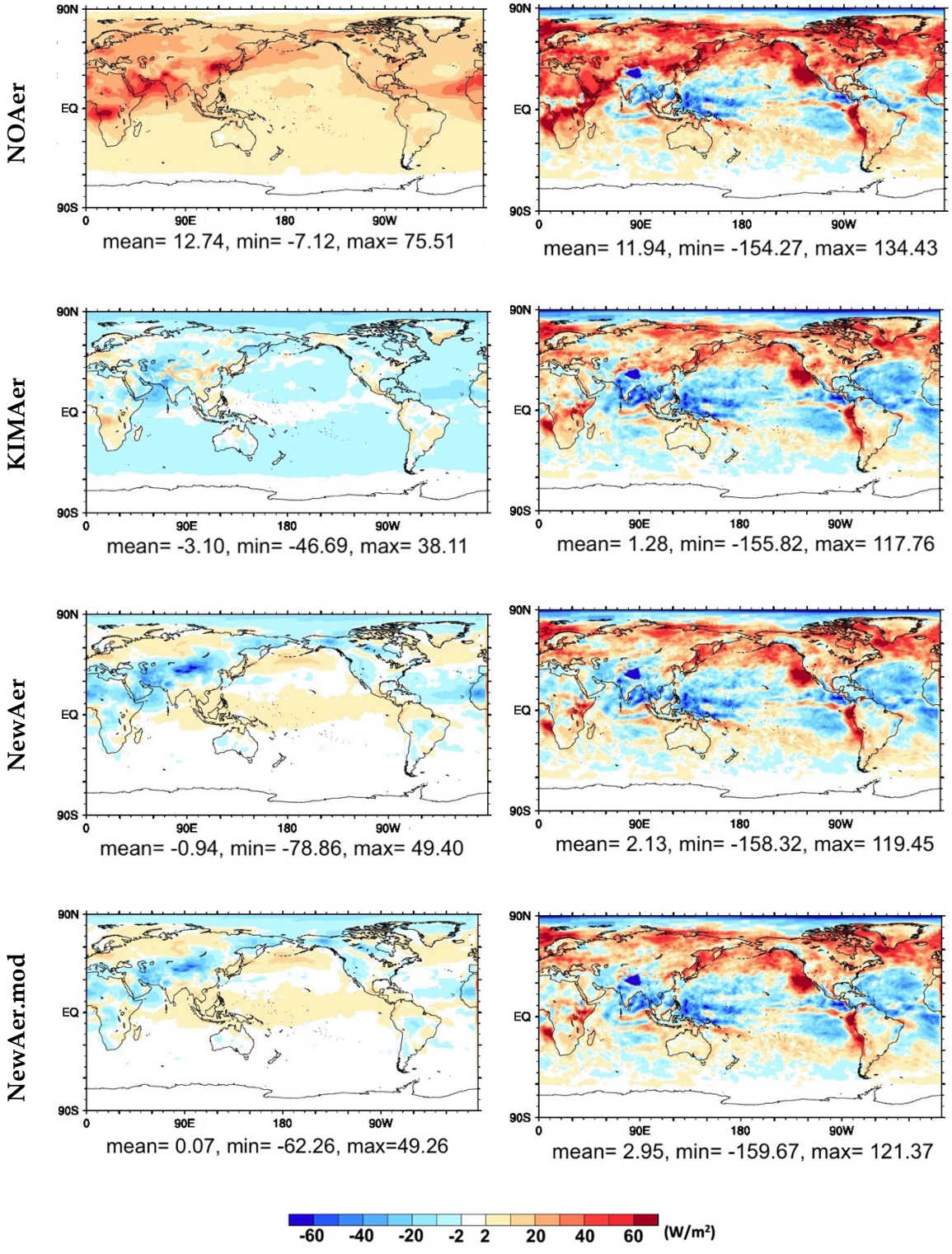

Figure 10. Global distributions of differences in SW downward fluxes (W/m^2) at the surfaces in clear sky (the first column) and all-sky (the second column) from Clouds and Earth's Radiant Energy System (CERES) in July 2017 among **NOAer**, **KIMAer**, **NewAer**, and **NewAer.mod**.

Table 5. The global means of biases and RMSEs of modeled SW downward fluxes (W/m^2) against CERES in July 2017.

Sky Condition	Statistics	NOAer	KIMAer	NewAer	NerAer.mod
Clear-sky	bias	12.74	−3.10	−0.94	0.07
	RMSE	13.73	7.00	6.59	6.18
All-sky	bias	11.94	1.28	2.13	2.95
	RMSE	41.16	36.86	37.01	37.01

In all-sky radiation, the biases against CERES included model biases caused by clouds and precipitation. **NOAer** had the positive biases in continents of NH and the west coast of South America, and the negative biases in the ocean at ITCZ and the Arctic sea. When the KIM in all-sky was compared with the KIM in clear-sky, the KIM seemed to underestimate clouds over the continents, but it overestimated over the tropical oceans. The global bias distribution patterns in all-sky seemed to be similar among the four cases. The ERFari in the KIM improved the biases in continents, but it did not drastically affect biases in the ocean and enhanced negative biases in the ITCZ. The global mean RMSEs in the experiment with aerosol climatology decreased only by 10% as compared with those in **NOAer** while the global mean biases decreased by more than 75% (Table 4). The biases in the continents and the north Pacific improved most in **NewAer.mod**, and global mean biases were the smallest in **KIMAer** due to smaller positive biases in the high latitude than in the other two aerosol cases.

Under such radiative fluxes modified by aerosols, the 10-day forecasts were verified with radiosonde data of GPH, temperature, specific humidity, and wind speed (Figure 11). In this study, the changes in specific humidity and wind speed due to aerosols were negligible. In **NOAer**, GPH had the negative biases at the upper and lower atmospheres after the fifth-day forecasts. Positive biases appeared in the mid-atmosphere in Asia in the early days of forecasts and the upper atmosphere in the tropics after fifth-day forecasts. The biases of temperature in **NOAer** had similar vertical stratification to those of GPH. However, the positive biases in temperature were located at lower altitudes than those in GPH were because temperature responses appeared closer to the aerosol source locations than GPH responses. On the reflection of the impacts of aerosol types on GPH and temperature in the sensitivity tests, BC and OM heated at the lower atmosphere, and dust and BC heated at the upper atmosphere (Figure 7c). BC aerosols also had dominant effects on positive changes of GPH (Figure 7d). It resulted in decreasing negative biases of temperature and GPH at the upper and lower atmospheres relative to **NOAer**. However, the positive biases at mid-atmosphere did not improve because the roles of absorbing aerosols seemed predominant in GPH and temperature. The opposite (positive and negative) biases seemed not significantly to change the global and 10-day means of the biases because they tended to cancel each other. Among the three aerosol experiments, the biases in GPH and temperature improved the most in **NewAer.mod**. The positive biases in the mid-atmosphere, which tended to be enhanced due to the existence of absorbing aerosols, were the smallest in **NewAer.mod**. The negative biases at the lower and upper atmospheres in **NewAer.mod** were larger than **KIMAer**; however, they were improved as compared with **NOAER**.

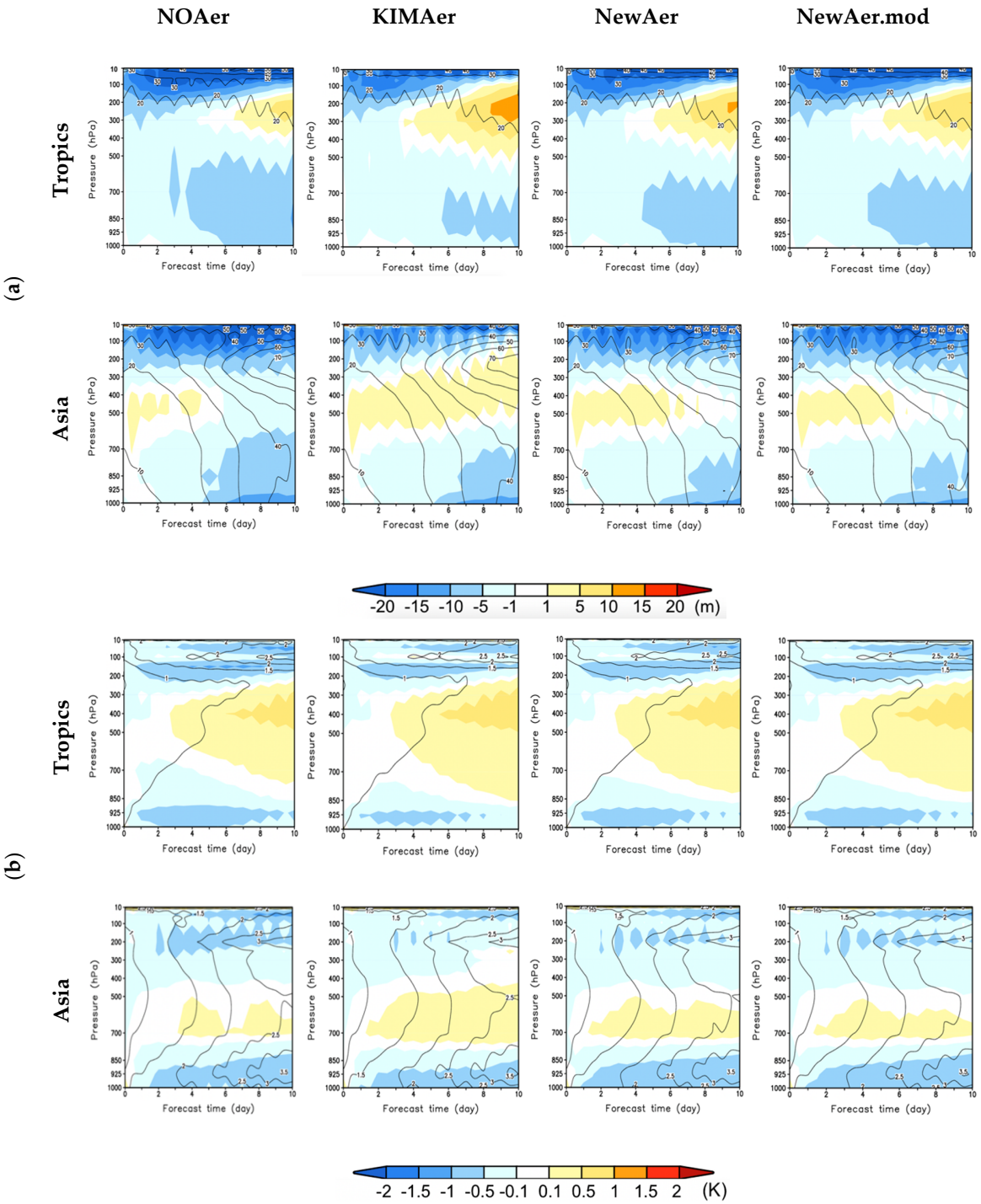

Figure 11. Time–pressure cross-section of biases (shading) and RMSEs (contours) of the (**a**) geopotential height (GPH) (m) and (**b**) temperature (K) for a 10-day forecast time computed against radiosonde data over Asia (25–65° N, 60–145° E) and the tropics (20° S–20° N, all longitude) in July 2017 in **NOAer, KIMAer, NewAer**, and **NewAer.mod.**

The statistical skill scores for the precipitation were calculated against observations such as the CPC unified gauge-based precipitation analysis, the TMPA, and the AWS data. The CPC and TMPA were used for the global precipitation in continents and ocean, respectively, and the AWS was used for the regional precipitation over the Korean Peninsula. However, the verification results were very similar, and the AWS was the most distinct among the three observations. **NOAer** showed the overestimation in weak (~5 mm/d) or moderate (10–15 mm/d) precipitation but the underestimation

in heavy (~20 mm/d) precipitation. It turned out that aerosols unilaterally reduced precipitation, and thus, they weakened positive biases in weak and moderate precipitation but enhanced negative biases in heavy precipitation. On the other hand, the Equitable Threat Score (ETS) that validates the accuracy of forecasts without contribution from the hit by chance in random forecast [73], improved in the three aerosol experiments as compared with the **NOAer**. Figure 12 showed the bias and ETS in the verification of all the experiments with AWS in the Korean peninsula. Among the three experiments with aerosols, **NewAer** showed the best performance in weak and moderate precipitation, and **KIMAer** made better performance in heavy precipitation than the other experiments. In the changes in surface precipitation by aerosols, PRECL was reduced by all aerosol types, whereas PRECC was reduced by only absorbing aerosols (Figure 9). Since the changes in concentration of absorbing aerosols tended to affect both PRECC and PRECL, absorbing aerosols were expected to enhance biases in the heavy precipitation. In the global distribution of precipitation biases to CPC or TMPA, **NOAer** overestimated precipitation in the continent and at high latitudes and underestimated in the tropical regions. Aerosols weakened the overestimation at high latitude, central Africa, and northmost of South America due to BC and OM. However, the underestimation in Southeast Asia was enhanced by carbonaceous aerosols (not shown here).

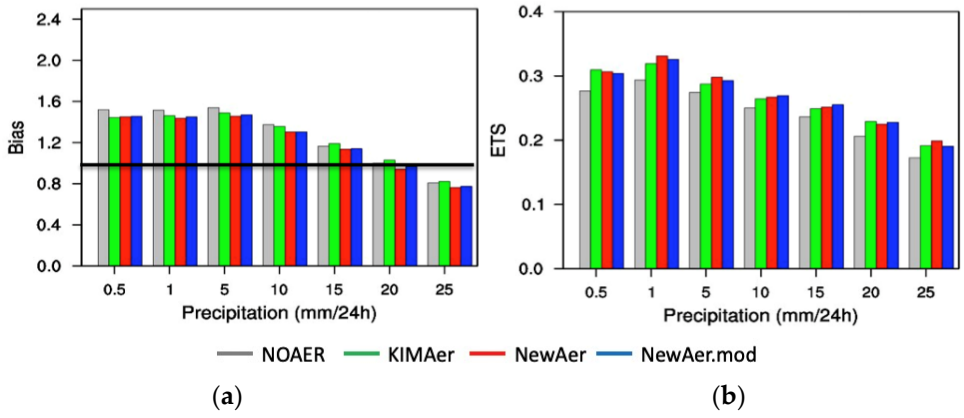

Figure 12. (**a**) Bias and (**b**) Equitable Threat Score (ETS) for 10-day averaged precipitation forecasts against Automatic Weather Station (AWS) over the Korean Peninsula in July of 2017. The solid horizontal line in (**a**) indicates the bias of 1, which means no bias.

In order to assess the statistical scores in weather forecasts, we calculated anomaly correlation (AC), root mean square error (RMSE), and skill score (SS) against the KIM self-analysis fields in GPH, temperature, relative humidity, and wind speed. The highlight of statistical analyses in this study were shown in Figure 13. The forecast scores with aerosols were not very different from those without aerosols. Nevertheless, GPH improved in the RMSEs at the upper atmosphere of NH, the SS at the high latitude, and the AC at the 500 hPa. The AC of mean sea level pressure also improved. On the other hand, forecast scores in SH became worse, such as the ACs of temperature at lower and upper atmospheres and the AC of GPH at the upper atmosphere. As shown in the sensitivity test of thermodynamic fields to aerosol types (Section 4), the changes in GPH profiles resulted mainly from BC and dust aerosols. Double-peak temperature profiles by BC and dust aerosols (Figure 7c), caused overheating at the lower and upper atmospheres. It led to decreasing in the AC of temperature at tropics and SH. The accumulated information of such temperature anomalies made the AC of GPH decrease at the upper atmosphere of SH. On the other hand, sea salts from vast oceans in SH seemed to play an additional role in the current NWPs besides ARI.

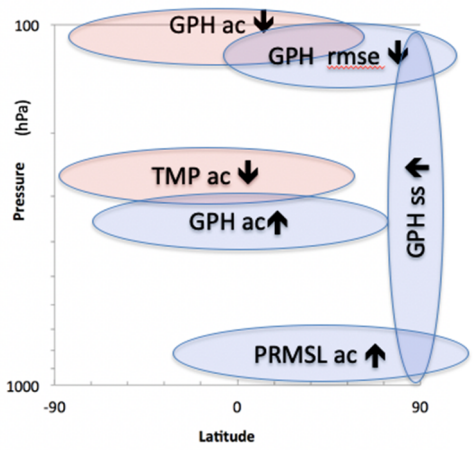

Figure 13. Schematic diagram in the highlight of statistical analyses in a medium-range forecast of **NewAer** in July of 2017.

Through ARI, aerosols worked unilaterally to decrease SW downward radiation at the surface, increase GPH and temperature, and decrease precipitation relative to aerosol-free atmosphere. The light-absorption capacity of aerosols played essential roles in weather forecasts. It led to weakening positive biases in SW downward radiation at the surface but occurring negative biases in dust and BC source regions; improving negative biases in GPH and temperature at the upper and lower atmospheres but worsening positive biases in the mid-atmosphere; reducing positive biases in weak and moderate precipitation but enhancing negative biases in heavy precipitation.

Those biases imply that there is room for the processes associated with the ERFari, such as aging and mixing of aerosol types and aerosol spectral optical properties in longwave radiations. Aerosol loading can be replaced with near-real-time (NRT)—base scenario in the specific or severe aerosol events. In the weather effects of ERFari, aerosols unilaterally changed the biases of the global forecast models, resulting in improving or exacerbating the biases of thermodynamic fields. Therefore, missing processes such as the aerosol–cloud interactions are likely to change the biases distribution patterns in the all-sky radiative fluxes and the tendency of reduction in cloud and precipitation.

This study suggests that *Newaerclim.mod* is the most desirable to use in the KIM among the three aerosol climatology data even though it does not drastically improve weather forecast scores as compared with the other two. Because it is a well-posed aerosol climatology, that is logical and consistent between aerosol loading and single-particle characteristics, and as realistic and recent as possible. Thus, *Newaerclim.mod* makes it easier to improve further bias corrections with the science-base and extend to the other aerosol roles in the hydrological cycles, surface albedo, and atmospheric chemistry, with consistency.

6. Conclusions

The roles of aerosols in NWP models were investigated by using well-posed aerosol data in Korean Integrated Model. The ARDF was calculated for a 10-day forecast on 1 July and 1 January 2017. In July, the ADRFs were larger than those in January, by a factor of 1.3, 2.1, and 1.6 at TOA, ATM, and SFC, respectively. To use a more distinct signal for the responses of thermodynamic and hydrometeor fields to individual aerosols, we carried out a sensitivity test for July. The medium-range weather forecasts with 31 ensemble simulations in July 2017 were verified with observations, and the model biases and the performances in weather forecasts were assessed in the cases of **NOAer, KIMAer, NewAer**, and **NewAer.mod**. We found the roles of individual aerosols in weather effects through the linkage between the sensitivity test and weather forecast performances.

- Well-posed aerosol climatology was constructed by implementing Mie calculation of individual aerosols and their aerosol loading data to radiative transfer modules. Monthly variations of

AOD were simulated well in terms of the peaks of individual aerosol types and relative ratios among aerosol species. The representative agents of July ADRF were dust at the surface and the atmosphere, and sulfate at the top of the atmosphere, respectively.

- Negative ADRFs at the surface had an impact on decreasing in sensible and latent heat fluxes at the surface. Positive ADRFs in the atmosphere caused the differences in atmospheric thermodynamic and hydrometeor fields relative to the aerosol-free conditions. The sensitivity tests showed that double-positive maxima in temperature were due to dust and BC, and wet surface and dry above in moisture mainly due to dust. Also, decreasing in cloud liquid or ice contents but a sharp positive layer of cloud liquid contents at 900 hPa were due to dust, BC, and OM. Through ARIs, aerosols tended to change the vertical gradients of temperature and humidity and to stabilize the atmosphere, leading to making the atmosphere with fewer clouds and less precipitation with respect to **noaer**. The differences due to individual aerosols were linearly additive to those due to total aerosols in heat fluxes, heating rates, humidity, and PRECC; however, they have not additive linearity to the differences due to total aerosols in temperature, geopotential height, and cloud liquid or ice contents, and PRECL. Dust was the most influential among absorbing and nonabsorbing aerosols, on the direct and semidirect effects of aerosols in July.
- Through ARI, aerosols worked unilaterally to decrease SW downward radiation at the surface, increase GPH and temperature, and decrease precipitation relative to aerosol-free atmosphere. The capacity of absorbing light due to aerosols played essential roles in weather forecasts. The verification of medium-range forecasts revealed that aerosols weakened positive biases in SW downward radiation but occurred negative biases in dust and BC source regions. Aerosols improved negative biases in GPH and temperature at the upper and lower atmospheres but worsened positive biases in the mid-atmosphere due to absorbing aerosols. Moreover, they reduced positive biases in weak and moderate precipitation but enhanced negative biases in heavy precipitation mainly due to absorbing aerosols. According to the sensitivity test of hydrometeor fields and the global distribution of precipitation biases, dust and OM weakened the overestimation at high latitude, central Africa, and northmost of South America. In contrast, BC and sea salt enhanced the underestimation in southeast Asia and the southern Indian Ocean, respectively.
- It turned out that weather forecast scores, including current aerosol information, improved in GPH of NH, however, they got worse in temperature of SH and GPH at the upper atmosphere of SH.

The current well-posed aerosol climatology can extend to more realistic descriptions of aerosol optical properties such as aging processes, mixing states, and spectral optical properties in the longwave radiation. Among the three aerosol climatology data, *Newaerclim.mod* is the most desirable data for the KIM in terms of the well-posed data frame, the bias corrections in the KIM with the science-base, and potential in cooperating with various physical and chemical aspects in NWP systems. It is worthy that prognostic aerosols produce the near-real-time (NRT) aerosol distribution and much more accurate aerosol radiative forcing when severe aerosol events break out. Moreover, they make it possible to execute the radiative forcing from aerosol–cloud interactions (RFaci) that should be included in the NWP models.

Funding: This research received no external funding. This work was supported by the R&D project on the development of global numerical weather prediction systems of the Korea Institute of Atmospheric Prediction Systems (KIAPS) funded by the Korea Meteorological Administration (KMA).

Acknowledgments: The author is grateful for computing resources at KMA supercomputers and KIAPS clusters. The KIM model is developed by a consortium composed of KIAPS, KMA. The authors also acknowledge MODIS, AERONET, MISR teams. I would like to thank Alissio Bozzo (EMES) for providing me with CAMSiRA data. I would like to thank Irina Sokolik with refractive index data. I also would like to thank you for the helpful discussion with Olivier Boucher (ILPS) and Chien Wang (CNRS). We appreciate the PIs and Co-I's and their staff for establishing and maintaining the AERONET sites used in this investigation.

Conflicts of Interest: The authors declare no conflict of interest.

Appendix A

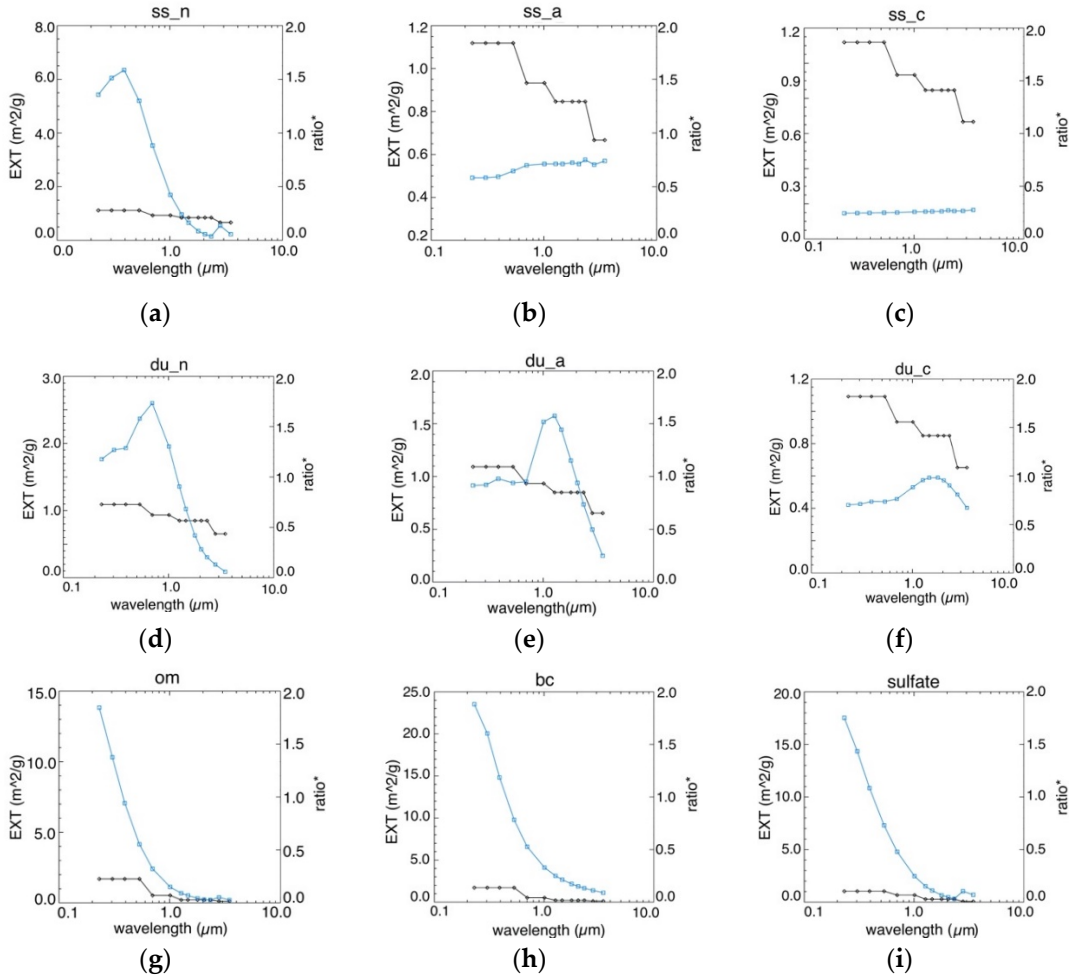

Figure A1. Aerosol spectral extinction characteristics. Blue color indicated mass extinction coefficients (m^2/g) in *Newaerclim* (blue color) of aerosol types such as sea salt ((**a**) nucleation, (**b**) accumulation, (**c**) coarse), dust ((**d**) nucleation, (**e**) accumulation, (**f**) coarse), (**g**) organic matter, (**h**) black carbon, and (**i**) sulfate. Black color indicates the ratio* which is the relative ratio of the inverse of AOD at 550 nm in *Kimaerclim*, of aerosol types such as (**a**–**c**) maritime, (**d**–**f**) desert, (**g**) continental, (**h**) urban, and (**g**) stratospheric volcano.

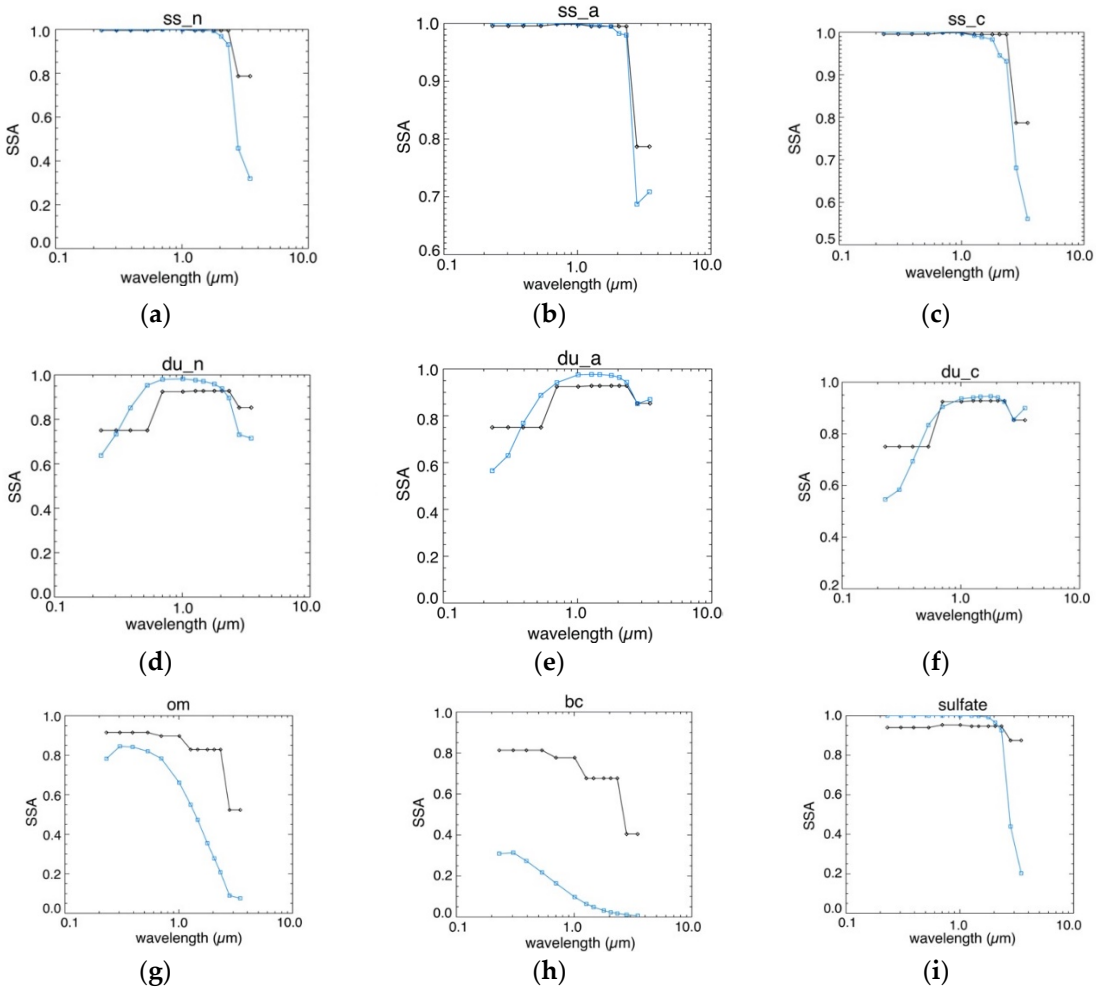

Figure A2. The same as Figure A1a–i but single scattering albedo. Black color indicates *Kimaerclim* and blue color indicates *Newaerclim*.

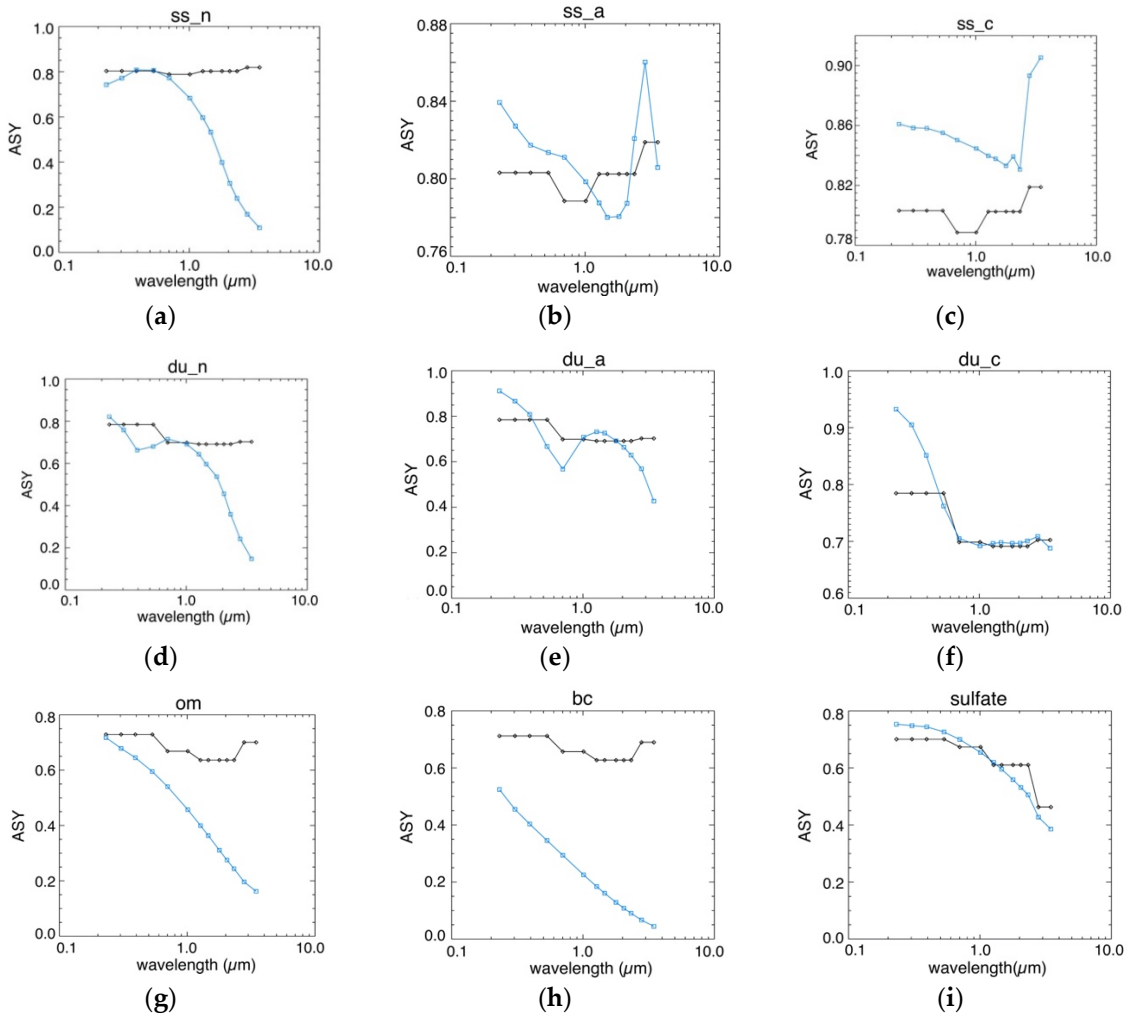

Figure A3. The same as Figure A1a–i but Asymmetric parameter. Black color indicates *Kimaerclim* and blue color indicates *Newaerclim*.

References

1. Intergovernmental Panel on Climate Change. Clouds and Aerosols. In *Climate Change 2013: The Physical Science Basis: Working Group I Contribution to the Fifth Assessment Report of the Intergovernmental Panel on Climate Change*; Cambridge University Press: Cambridge, UK; New York, NY, USA, 2014; pp. 571–658.
2. Haywood, J.; Boucher, O. Estimates of the direct and indirect radiative forcing due to tropospheric aerosols. A review. *Rev. Geophys.* **2000**, *38*, 513–543. [CrossRef]
3. Boucher, O. *Atmospheric Aerosols: Properties and Climate Impacts*; Springer: Berlin, Germany, 2015; pp. 227–246.
4. WMO, Aerosols and Climate, WCP 12 (World Climate Research Program Report No. 12), 1980, International Council of Scientific Unions. Available online: https://library.wmo.int/index.php?lvl=author_see&id=11424#.Xv3BEpMzai4 (accessed on 17 June 2020).
5. Wang, C. Anthropogenic aerosols and the distribution of past large-scale precipitation change. *Geophys. Res. Lett.* **2015**, *42*, 10876–10884. [CrossRef] [PubMed]
6. Charlson, R.J.; Langner, J.; Rodhe, H.; Leovy, C.B.; Warren, S.G. Perturbation of the northern hemisphere radiative balance by backscattering from anthropogenic sulfate aerosols. *Tellus A Dyn. Meteorol. Oceanogr.* **1991**, *43*, 152–163. [CrossRef]
7. Kiehl, J.T.; Briegleb, B.P. The Relative Roles of Sulfate Aerosols and Greenhouse Gases in Climate Forcing. *Science* **1993**, *260*, 311. [CrossRef] [PubMed]
8. Wang, C.; Kim, D.; Ekman, A.M.L.; Barth, M.C.; Rasch, P.J. Impact of anthropogenic aerosols on Indian summer monsoon. *Geophys. Res. Lett.* **2009**, *36*, L21704. [CrossRef]

9. Intergovernmental Panel on Climate Change. Anthropogenic and Natural Radiative Forcing. In *Climate Change 2013: The Physical Science Basis: Working Group I Contribution to the Fifth Assessment Report of the Intergovernmental Panel on Climate Change*; Cambridge University Press: Cambridge, UK; New York, NY, USA, 2014; pp. 659–740.
10. Baker, L.H.; Collins, W.J.; Olivié, D.J.L.; Cherian, R.; Myhre, G.; Quaas, J. Climate responses to anthropogenic emissions of short-lived climate pollutants. *Atmos. Chem. Phys.* **2015**, *15*, 8201–8216. [CrossRef]
11. Shindell, D.; Schulz, M.; Ming, Y.; Takemura, T.; Faluvegi, G.; Ramaswamy, R. Spatial scales of climate response to inhomogeneous radiative forcing. *J. Geophys. Res.* **2010**, *115*, D19110. [CrossRef]
12. Undorf, S.; Polson, D.; Bollasina, M.A.; Ming, Y.; Schurer, A.; Hegerl, G.C. Detectable Impact of Local and Remote Anthropogenic Aerosols on the 20th Century Changes of West African and South Asian Monsoon Precipitation. *J. Geophys. Res. Atmos.* **2018**, *123*, 4871–4889. [CrossRef]
13. Westervelt, D.M.; Conley, A.J.; Fiore, A.M.; Lamarque, J.-F.; Shindell, D.T.; Previdi, M.; Mascioli, N.R.; Faluvegi, G.; Correa, G.; Horowitz, L.W. Connecting regional aerosol emissions reductions to local and remote precipitation responses. *Atmos. Chem. Phys.* **2018**, *18*, 12461–12475. [CrossRef]
14. Liu, L.; Shawki, D.; Voulgarakis, A.; Kasoar, M.; Samset, B.H.; Myhre, G.; Forster, P.M.; Hodnebrog, Ø.; Sillmann, J.; Aalbergsjø, S.G.; et al. A PDRMIP Multimodel Study on the Impacts of Regional Aerosol Forcings on Global and Regional Precipitation. *J. Clim.* **2018**, *31*, 4429–4447. [CrossRef]
15. Krishnan, R.; Sabin, T.P.; Vellore, R.; Mujumdar, M.; Sanjay, J.; Goswami, B.N.; Hourdin, F.; Dufresne, J.-L.; Terray, P. Deciphering the desiccation trend of the South Asian monsoon hydroclimate in a warming world. *Clim. Dyn.* **2016**, *47*, 1007–1027. [CrossRef]
16. Dong, B.; Sutton, R.T.; Highwood, E.J.; Wilcox, L.J. Preferred response of the East Asian summer monsoon to local and non-local anthropogenic sulphur dioxide emissions. *Clim. Dyn.* **2016**, *46*, 1733–1751. [CrossRef]
17. Bartlett, R.E.; Bollasina, M.A.; Booth, B.B.B.; Dunstone, N.J.; Marenco, F.; Messori, G.; Bernie, D.J. Do differences in future sulfate emission pathways matter for near-term climate? A case study for the Asian monsoon. *Clim. Dyn.* **2018**, *50*, 1863–1880. [CrossRef]
18. Tang, T.; Shindell, D.; Samset, B.H.; Boucher, O.; Forster, P.M.; Hodnebrog, Ø.; Myhre, G.; Sillmann, J.; Voulgarakis, A.; Andrews, T.; et al. Dynamical response of Mediterranean precipitation to greenhouse gases and aerosols. *Atmos. Chem. Phys.* **2018**, *18*, 8439–8452. [CrossRef]
19. Hodnebrog, Ø.; Myhre, G.; Forster, P.M.; Sillmann, J.; Samset, B.H. Local biomass burning is a dominant cause of the observed precipitation reduction in southern Africa. *Nat. Commun.* **2016**, *7*, 11236. [CrossRef] [PubMed]
20. Bozzo, A.; Remy, S.; Benedetti, A.; Flemming, J.; Bechtold, P.; Rodwell, M.J.; Morcrette, J.-J. *Implementation of a CAMS-Based Aerosol Climatology in the IFS*; ECMWF Tech. Memo. 801: Reading, UK, 2017; Available online: https://www.ecmwf.int/sites/default/files/elibrary/2017/17219-implementation-cams-based-aerosol-climatology-ifs.pdf (accessed on 1 October 2019).
21. Mulcahy, J.P.; Walters, D.N.; Bellouin, N.; Milton, S.F. Impacts of increasing the aerosol complexity in the Met Office global numerical weather prediction model. *Atmos. Chem. Phys.* **2014**, *14*, 4749–4778. [CrossRef]
22. Baklanov, A.; Brunner, D.; Carmichael, G.; Flemming, J.; Freitas, S.; Gauss, M.; Hov, Ø.; Mathur, R.; Schlünzen, K.; Seigneur, C.; et al. Key Issues for Seamless Integrated Chemistry-Meteorology Modeling. *Bull. Am. Meteorol. Soc.* **2018**, *98*, 2285–2292. [CrossRef]
23. Bozzo, A.; Benedetti, A.; Flemming, J.; Kipling, Z.; Rémy, S. An aerosol climatology for global models based on the tropospheric aerosol scheme in the Integrated Forecasting System of ECMWF. *Geosci. Model Dev.* **2020**, *13*, 1007–1034. [CrossRef]
24. Toll, V.; Reis, K.; Ots, R.; Kaasik, M.; Männik, A.; Prank, M.; Sofiev, M. SILAM and MACC reanalysis aerosol data used for simulating the aerosol direct radiative effect with the NWP model HARMONIE for summer 2010 wildfire case in Russia. *Atmos. Environ.* **2015**, *121*, 75. [CrossRef]
25. Zhang, J.; Reid, J.S.; Christensen, M.; Benedetti, A. An evaluation of the impact of aerosol particles on weather forecasts from a biomass burning aerosol event over the Midwestern United States: Observational-based analysis of surface temperature. *Atmos. Chem. Phys.* **2016**, *16*, 6475–6494. [CrossRef]
26. Tompkins, A.M.; Cardinali, C.; Morcrette, J.-J.; Rodwell, M. Influence of aerosol climatology on forecasts of the African easterly jet. *Geophys. Res. Lett.* **2005**, *32*, L10801. [CrossRef]

27. Rémy, S.; Benedetti, A.; Bozzo, A.; Haiden, T.; Jones, L.; Razinger, M.; Flemming, J.; Engelen, R.J.; Peuch, V.H.; Thepaut, J.N. Feedbacks of dust and boundary layer meteorology during a dust storm in the eastern Mediterranean. *Atmos. Chem. Phys.* **2015**, *15*, 12909–12933. [CrossRef]
28. Rodwell, M.J.; Jung, T. Understanding the local and global impacts of model physics changes: An aerosol example. *Q. J. R. Meteorol. Soc.* **2008**, *134*, 1479. [CrossRef]
29. Reale, O.; Lau, K.M.; Da Silva, A. Impact of Interactive Aerosol on the African Easterly Jet in the NASA GEOS-5 Global Forecasting System. *Weather. Forecast.* **2011**, *26*, 504–519. [CrossRef]
30. Morcrette, J.-J.; Benedetti, A.; Ghelli, A.; Kaiser, J.W.; Tompkins, A.M. *Aerosol-Cloud-Radiation Interactions and their Impact on ECMWF/MACC Forecasts*; ECMWF: Reading, UK, 2011.
31. Toll, V.; Gleeson, E.; Nielsen, K.P.; Männik, A.; Mašek, J.; Rontu, L.; Post, P. Impacts of the direct radiative effect of aerosols in numerical weather prediction over Europe using the ALADIN-HIRLAM NWP system. *Atmos. Res.* **2016**, *172*, 163–173. [CrossRef]
32. Choi, I.-J.; Park, R.-S.; Lee, J. Impacts of a newly-developed aerosol climatology on numerical weather prediction using a global atmospheric forecasting model. *Atmos. Environ.* **2019**, *197*, 77–91. [CrossRef]
33. D'Almeida, G.A.; Koepke, P.; Shettle, E.P. *Atmospheric Aerosols(Global Climatology and Radiative Characteristics)*; A Deepak Publishing: Hampton, VA, USA, 1991.
34. Hess, M.; Koepke, P.; Schult, I. Optical Properties of Aerosols and Clouds: The Software Package OPAC. *Bull. Am. Met. Soc.* **1998**, *79*, 831–844. [CrossRef]
35. Eskes, H.; Huijnen, V.; Arola, A.; Benedictow, A.; Blechschmidt, A.-M.; Botek, E.; Boucher, O.; Bouarar, I.; Chabrillat, S.; Cuevas, E.; et al. Validation of reactive gases and aerosols in the MACC global analysis and forecast system. *Geosci. Model Dev.* **2015**, *8*, 3523–3546. [CrossRef]
36. Emmons, L.K.; Walters, S.; Hess, P.G.; Lamarque, J.-F.; Pfister, G.G.; Fillmore, D.; Granier, C.; Guenther, A.; Kinnison, D.; Laepple, T.; et al. Description and evaluation of the model for ozone and related chemical tracers, version 4 (MOZART-4). *Geosci. Model Dev.* **2010**, *3*, 43–67. [CrossRef]
37. Tanré, D.; Geleyn, J.-F.; Slingo, J. First results of the introduction of an advanced aerosol-radiation interaction in the ECMWF low resolution global model. In *Aerosols and Their Climatic Effects*; Gerber, H., Deepak, A., Eds.; A Deepak Publ: Hampton, VA, USA, 1984; pp. 133–177.
38. WMO/IAMAP, Radiation Commission, A Preliminary Cloudless Standard Atmosphere for Radiation Computation, WMO/TD-NO.24; WCP- No. 112, International Council of Science Union, 1984. Available online: https://library.wmo.int/doc_num.php?explnum_id=4988 (accessed on 17 June 2020).
39. Sinyuk, A.; Torres, O.; Dubovik, O. Combined use of satellite and surface observations to infer the imaginary part of refractive index of Saharan dust. *Geophys. Res. Lett.* **2003**, *30*, 53. [CrossRef]
40. Drury, E.; Jacob, D.J.; Spurr, R.J.; Wang, J.; Shinozuka, Y.; Anderson, B.E.; Clarke, A.D.; Dibb, J.; McNaughton, C.; Weber, R. Synthesis of satellite (MODIS), aircraft (ICARTT), and surface (IMPROVE, EPA-AQS, AERONET) aerosol observations over eastern North America to improve MODIS aerosol retrievals and constrain surface aerosol concentrations and sources. *J. Geophys. Res.* **2010**, *115*, D14204. [CrossRef]
41. Flemming, J.; Benedetti, A.; Inness, A.; Engelen, R.J.; Jones, L.; Huijnen, V.; Remy, S.; Parrington, M.; Suttie, M.; Bozzo, A.; et al. The CAMS interim Reanalysis of Carbon Monoxide, Ozone and Aerosol for 2003–2015. *Atmos. Chem. Phys.* **2017**, *17*, 1945. [CrossRef]
42. Hong, S.-Y.; Park, S.K.; Park, R.; Dudhia, J. Korean Global Data Assimilation and Prediction System. *AsiaPac. J. Atmos. Sci.* **2018**, *54*, 265. [CrossRef]
43. Bohren, C.F.; Huffman, D.R. *Absorption and Scattering of Light by Small Particles*; Wiley Science Paperback Series: New York, NY, USA, 1998; p. 544.
44. Toon, O.B.; Ackerman, T.P. Algorithms for the calculation of scattering by stratified sphere. *Appl. Opt.* **1981**, *20*, 3657–3660. [CrossRef] [PubMed]
45. Wiscombe, W.J. Improved Mie scattering algorithms. *Appl. Opt.* **1980**, *19*, 1505–1509. [CrossRef] [PubMed]
46. Jeong, G.-R.; Sokolik, I.N. Effect of mineral dust aerosols on the photolysis rates in the clean and polluted marine environments. *J. Geophys. Res.* **2007**, *112*, D21308. [CrossRef]
47. Lesins, G.; Chylek, P.; Lohmann, U. A study of internal and external mixing scenarios and its effect on aerosol optical properties and direct radiative forcing. *J. Geophys. Res.* **2002**, *107*, 4094. [CrossRef]
48. Bond, T.C.; Habib, G.; Bergstrom, R.W. Limitations in the enhancement of visible light absorption due to mixing state. *J. Geophys. Res.* **2006**, *111*, D20211. [CrossRef]

49. Kim, D.; Wang, C.; Ekman, A.M.L.; Barth, M.C.; Lee, D.-I. The responses of cloudiness to the direct radiative effect of sulfate and carbonaceous aerosols. *J. Geophys. Res. Atmos.* **2014**, *119*, 1172. [CrossRef]
50. Woodward, S. Modeling the atmospheric life cycle and radiative impact of mineral dust in the Hadley Centre climate model. *J. Geophys. Res.* **2001**, *106*, 18155–18166. [CrossRef]
51. Lacis, A. Refractive Indices of Three Hygroscopic Aerosols and Their Dependence on Relative Humidity, 2001. Available online: https://gacp.giss.nasa.gov/datasets/lacis/introduction.pdf (accessed on 1 June 2020).
52. Remer, L.A.; Kaufman, Y.J.; Tanré, D.; Mottoo, S.; Chu, D.A.; Martins, J.V.; Li, R.-R.; Ichoku, C.; Levy, R.C.; Kleidman, R.G.; et al. The MODIS aerosol algorithm, products, and validation. *J. Atmos. Sci.* **2005**, *62*, 947–973. [CrossRef]
53. Kahn, R.A.; Gaitley, B.J.; Garay, M.J.; Diner, D.J.; Eck, T.F.; Smirnov, A.; Holben, B.N. Multiangle Imaging SpectroRadiometer global aerosol product assessment by comparison with the Aerosol Robotic Network. *J. Geophys. Res.* **2010**, *115*, D23209. [CrossRef]
54. Baek, S. A revised radiation package of G-packed McICA and two-stream ap- proximation: Performance evaluation in a global weather forecasting model. *J. Adv. Model. Earth Syst.* **2017**, *9*, 1628–1640. [CrossRef]
55. Ek, M.B.; Mitchell, K.E.; Lin, Y.; Rogers, E.; Grunmann, P.; Koren, V.; Gayno, G.; Tarpley, J.D. Implementation of noah land surface model advances in the national Centers for environmental prediction operational mesoscale eta model. *J. Geophys. Res.* **2003**, *108*, 8851. [CrossRef]
56. Hong, S.-Y. A new stable boundary-layer mixing scheme and its impact on the simulated East Asian summer monsoon. *Quart. J. Roy. Meteor. Soc.* **2010**, *136*, 1481–1496. [CrossRef]
57. Choi, H.-J.; Hong, S.-Y. An updated subgrid orographic parameterization for global atmospheric forecast. *J. Geophys. Res. Atmos.* **2015**, *120*, 12445–12457. [CrossRef]
58. Han, J.-Y.; Hong, S.-Y.; Lim, K.-S.S.; Han, J. Sensitivity of a cumulus parameterization scheme to precipitation production representation and its impact on a heavy rain event over Korea. *Mon. Weather Rev.* **2016**, *144*, 2125–2135. [CrossRef]
59. Hong, S.-Y.; Park, H.; Cheong, H.-B.; Kim, J.-E.; Koo, M.-S.; Jang, J.; Ham, S.; Hwang, S.-O.; Park, B.-K.; Chang, E.-C.; et al. The global/regional integrated model system (GRIMs). *Asia Pac. J. Atmos. Sci.* **2013**, *49*, 219–243. [CrossRef]
60. Hong, S.-Y.; Duhdia, J.; Chen, S.-H. A revised approach to ice- microphysical processes for the bulk parameterization of cloud and precipitation. *Mon. Weather Rev.* **2004**, *132*, 103–120. [CrossRef]
61. Bae, S.Y.; Hong, S.-Y.; Lim, K.-S.S. Coupling WRF double-moment 6-class micro- physics schemes to RRTMG radiation scheme in weather research forecasting model. *Adv. Meteorol.* **2016**. [CrossRef]
62. Park, R.-S.; Chae, J.-H.; Hong, S.-Y. A revised prognostic cloud fraction scheme in a global forecasting system. *Mon. Weather Rev.* **2016**, *114*, 1219–1229. [CrossRef]
63. Copernicus Climate Change Service (C3S) (2017): ERA5: Fifth Generation of ECMWF Atmospheric Reanalyses of the Global Climate. Copernicus Climate Change Service Climate Data Store (CDS). Available online: https://cds.climate.copernicus.eu/cdsapp#!/home (accessed on 1 April 2020).
64. Kanamitsu, M. Description of the NMC global data assimilation and forecast system. *Weather. Forecast.* **1989**, *4*, 335–342. [CrossRef]
65. Xie, P. CPC Unified Gauge-Based Analysis of Global Daily Precipitation, the 90th American Meteorological Society Annual Meeting, 2010. Available online: https://climatedataguide.ucar.edu/climate-data/cpc-unified-gauge-based-analysis-global-daily-precipitation (accessed on 1 April 2020).
66. Huffman, G.J.; Bolvin, D.T.; Nelkin, E.J.; Wolff, D.B.; Adler, R.F.; Gu, G.; Hong, Y.; Bowman, K.P.; Stocker, E.F. The TRMM Multisatellite Precipitation Analysis (TMPA): Quasi-Global, Multiyear, Combined-Sensor Precipitation Estimates at Fine Scales. *J. Hydrometeor.* **2007**, *8*, 38–55. [CrossRef]
67. Myhre, G. 2009: Consistency between satellite-derived and modeled estimates of the direct aerosol effect. *Science* **2009**, *325*, 187–190. [CrossRef]
68. Bellouin, N.; Quaas, J.; Morcrette, J.-J.; Boucher, O. Estimates of aerosol radiative forcing from the MACC re-analysis. *Atmos. Chem. Phys.* **2013**, *13*, 2045–2062. [CrossRef]
69. Ghan, S.J.; Liu, X.; Easter, R.C.; Zaveri, R.; Rasch, P.J.; Yoon, J.-H.; Eaton, B. Toward a minimal representation of aerosols in climate models: Comparative decomposition of aerosol direct, semi-direct, and indirect radiative forcing. *J. Clim.* **2012**, *25*, 6461–6476. [CrossRef]

70. Lohmann, U.; Rotstayn, L.; Storelvmo, T.; Jones, A.; Menon, S.; Quaas, J.; Ekman, A.M.L.; Koch, D.; Ruedy, R. Total aerosol effect: Radiative forcing or radiative flux perturbation? *Atmos. Chem. Phys.* **2010**, *10*, 3235–3246. [CrossRef]
71. Jones, A.; Haywood, J.M.; Boucher, O. Aerosol forcing, climate response and climate sensitivity in the Hadley Centre climate model. *J. Geophys. Res.* **2007**, *112*, D20211. [CrossRef]
72. Persad, G.G.; Ming, Y.; Ramaswamy, V. Tropical Tropospheric-Only Responses to Absorbing Aerosols. *J. Clim.* **2012**, *25*, 2471–2480. [CrossRef]
73. Forecast User Guide, 6.4 Relative Skill of IFS Models. Available online: https://confluence.ecmwf.int/display/FUG/6.4+Relative+Skill+of+IFS+Models (accessed on 1 April 2020).